New submodel for emissions from Explosive Volcanic ERuptions (EVER v1.1) within the Modular Earth Submodel System (MESSy, version 2.55.1)

Matthias Kohl[1], Christoph Brühl[1], Jennifer Schallock[1], Holger Tost[2], Patrick Jöckel[3], Adrian Jost[4], Steffen Beirle[4], Michael Höpfner[5], and Andrea Pozzer[1,6]

[1]Atmospheric Chemistry Department, Max Planck Institute for Chemistry, Mainz, Germany
[2]Institute for Physics of the Atmosphere, Johannes Gutenberg University, Mainz, Germany
[3]Institut für Physik der Atmosphäre, Deutsches Zentrum für Luft- und Raumfahrt (DLR), Oberpfaffenhofen, Germany
[4]Satellite Remote Sensing, Max-Planck-Institut für Chemie, Mainz, Germany
[5]Institute of Meteorology and Climate Research, Karlsruhe Institute of Technology, Karlsruhe, Germany
[6]Climate and Atmosphere Research Center, The Cyprus Institute, Nicosia, Cyprus

Correspondence: Matthias Kohl (m.kohl@mpic.de)

Abstract. This work documents the operation of a new submodel for tracer emissions from Explosive Volcanic ERuptions (EVER v1.1), developed within the Modular Earth Submodel System (MESSy, version 2.55.1). EVER calculates additional tendencies of gaseous and aerosol tracers based on emission source parameters, aligned to specific sequences of volcanic eruptions or other atmospheric emission sources, and allowing various vertical emission profiles. We show that volcanic SO_2 plumes can be reasonably reproduced through EVER emissions in numerical simulations with the ECHAM/MESSy Atmospheric Chemistry Model (EMAC), using satellite observations of SO_2 columns and mixing ratios following the explosive eruption of the Nabro volcano (Eritrea) in 2011 and a degassing event of the Kilauea volcano (2018) in Hawaii. Previous volcanic studies showed large variability in stratospheric SO_2 burdens depending on the chosen volcanic emission databases and parameters. Sensitivity studies on SO_2 emissions from the Nabro volcano explore perturbations of the emission source parameters, revealing that emission altitude and the emitted mass above the tropopause are most important for the mid- to long-term evolution of stratospheric SO_2 plumes and the resulting stratospheric aerosol, while the correct timing and geographical location of the stratospheric entrance is crucial for the short-term plume evolution. We integrate information from a volcanic SO_2 emission inventory, additional satellite observations, and our findings from the sensitivity studies to establish a historical standard setup for volcanic eruptions impacting stratospheric SO_2 from 1990 to 2023. This setup was successfully evaluated with satellite observations of stratospheric SO_2 burden and aerosol optical properties. We advocate for this to be a standardized setup in all simulations within the MESSy framework concentrating on the upper troposphere and stratosphere in this period. Further potential applications of EVER involve studies on volcanic ash, wildfires, solar radiation modification, and atmospheric transport processes.

1 Introduction

Volcanic eruptions strongly impact atmospheric chemistry, climate dynamics, and air pollution. The most explosive eruptions reach the Upper Troposphere and Lower Stratosphere (UTLS), carrying primarily emitted particles (mostly volcanic ash) and volcanic gases, that lead to the formation and growth of aerosol particles. The resulting additional stratospheric aerosol loading may exert a negative radiative forcing (Schallock et al., 2023; Schmidt et al., 2018), and serves as surfaces for heterogeneous reactions, thus, impacting stratospheric composition in general and ozone in particular (e. g. Klobas et al., 2017; Tie and Brasseur, 1995). Moreover, in the troposphere, gaseous and particulate emissions from degassing volcanoes can affect the environment and public health via inhalation or acid rain (Durand and Grattan, 2001; Stewart et al., 2022).

Although volcanically emitted gases are typically dominated by water vapor and carbon dioxide, the respective total amount is mostly negligible[1] in comparison to global emissions and concentrations (Textor et al., 2004). However, in general, the third most abundant species in volcanic plumes, sulfur dioxide (SO_2), exerts the most significant impact on atmospheric chemistry and climate, substantially enriching atmospheric SO_2 levels (Textor et al., 2004). Subsequently, SO_2 undergoes oxidation to form sulfuric acid (H_2SO_4), which rapidly converts to the liquid aerosol phase under most atmospheric conditions (e. g. Kremser et al., 2016), but can also form solid salts depending on atmospheric conditions. We refer to "sulfur aerosol" as the sum of liquid and solid sulfur aerosol in the following.

The (global) impact of volcanic eruptions strongly depends on the strength of the eruption and its geographical location. SO_2 emissions from degassing volcanoes and smaller eruptions, failing to reach the stratosphere, primarily influence the local environment, as emitted species and their products are usually removed in the troposphere by rainout processes within weeks[2]. When volcanic SO_2 emissions reach the stratosphere, the subsequently formed sulfur aerosol enhances stratospheric aerosol and is distributed widely across the globe. The lifetime of stratospheric aerosol can exceed 2 years when injected in the tropics, leading to sustained impacts on atmospheric radiative balance and climate dynamics. The strongest eruption in recent times, Mount Pinatubo in 1991, significantly increased the stratospheric Aerosol Optical Depth (sAOD) and resulted in a radiative forcing of -3 to -5 Wm^{-2} (Schallock et al., 2023; Schmidt et al., 2018), comparable to the magnitude of positive anthropogenic radiative forcing attributed to greenhouse gas emissions (IPCC, 2021).

In addition to gaseous emissions, volcanic eruptions release varying amounts of primary aerosol, mainly consisting of volcanic ash, directly into the atmosphere. While the lifetime of ash particles in the atmosphere is relatively short, resulting in mostly negligible climate effects, recent studies have indicated that ash can persist in the atmosphere for longer durations than previously anticipated (Vernier et al., 2016). Furthermore, ash particles can interact with other atmospheric constituents, such as SO_2 and H_2SO_4, thereby influencing atmospheric chemistry (Zhu et al., 2020), and pose severe hazards to aviation and

[1] Notable exceptions arise during eruptions of submarine volcanoes, such as the Hunga Tonga-Hunga Ha'apai volcano in January 2022 (e. g. Vömel et al., 2022; Sellitto et al., 2022; Schoeberl et al., 2022; Xu et al., 2022), that can inject substantial amounts of water vapor into the stratosphere, thereby impacting climate, atmospheric dynamics, and radiative forcing.

[2] However, they can exert a strong risk for public health and even influence the short-term climate by altering cloud properties (e. g. the 2014-2015 fissure eruption in the Holuhraun vent of Bardarbunga, Iceland, leading to a global-mean radiative forcing of -0.2 Wm^{-2}; Malavelle et al., 2017)

affect public health and the environment, as they deposit on the Earth's surface (Durand and Grattan, 2001; Stewart et al., 2022).

The understanding of the aforementioned impacts of volcanic eruptions on climate and atmospheric chemistry heavily relies on atmospheric numerical modelling. Numerical simulations can study the impact of volcanoes on the radiative budget, atmospheric chemistry, and dynamics of the atmosphere. Furthermore, the incorporation of volcanic eruptions is indispensable for model-based studies on global atmospheric aerosol, particularly in comparison to observations from satellites and aircraft campaigns. Without accurate accounting for volcanic eruptions, models may underestimate upper tropospheric and stratospheric aerosol concentrations, thereby compromising the accuracy of simulated atmospheric aerosol distributions (e.g., Reifenberg et al., 2022). Thus, atmospheric models need the capability to account for gaseous and particulate volcanic emissions in general, and SO_2 in particular.

Volcanic SO_2 emission databases are the basis for the correct implementation of volcanic eruptions in atmospheric models. Timmreck et al. (2018) recommend four different emission inventories. Neely III and Schmidt (2016) and Mills et al. (2016) provide an inventory for tropospheric and stratospheric volcanoes, covering daily emissions and providing plume top and minimal height. Carn et al. (2017) provide a very detailed list of tropospheric and stratospheric volcanoes, however not distinguishing between the tropospheric and stratospheric part of the plume. Brühl et al. (2018) developed a volcanic SO_2 emission database from 1990 to 2021 (updated by Schallock et al., 2023), focusing only on the stratospheric part of the plume, also including smaller eruptions. Finally, the emission database from Diehl et al. (2012) only covers volcanoes up to 2010.

The treatment of SO_2 from volcanic eruptions based on the available emission inventories in global atmospheric models varies widely (e. g. Quaglia et al., 2023; Timmreck et al., 2018). Quaglia et al. (2023) performed a model intercomparison study focusing on the Pinatubo eruption, finding that inter- and intra-model differences in the response of SO_2 and sulfur aerosol on the Pinatubo eruption are large for a range of sensitivity experiments. The differences were mostly attributed to differing stratospheric transport, emission databases, aerosol microphysics and stratospheric chemistry. Vattioni et al. (2024) investigated the impact of microphysical settings within the SOCOL-AERv2 aerosol chemistry-climate model and found that the microphysical timestep, as well as the order of the microphysical processes can lead to vastly differing resulting stratospheric aerosol.

Brodowsky et al. (2021) studied small- and medium-sized volcanic eruptions from 2008 to 2012, investigating the sensitivity of the resulting aerosol burdens to the different emission databases, internal model variability, dynamic nudging and the vertical resolution. The largest uncertainties resulted from the emission databases and their application. Most volcanic model studies inject SO_2 in columns at the geographical location of the volcano (e. g. Quaglia et al., 2023; Mills et al., 2016; Schmidt et al., 2018; Brodowsky et al., 2021), however the vertical extent of the column is mostly unknown and depends on a number of assumptions. For instance, Brodowsky et al. (2021) emitted the recommended SO_2 amounts (for the emission inventories of Brühl et al., 2018; Carn et al., 2017; Diehl et al., 2012) from the prescribed plume top height down a third of the distance to the Earth's surface. However, this approach has to be aligned with the emission inventory derivation, i. e. if only the stratospheric plume is considered for the derived SO_2 mass (as in the database from Brühl et al. (2018)) or the tropospheric part of the plume as well (as in the databases from Carn et al. (2017) and Diehl et al. (2012)).

In this study, we expand the capabilities of the Modular Earth Submodel System, MESSy (version 2.55.1, Jöckel et al., 2010), to incorporate the seamless simulation of volcanic eruptions with a new submodel for Explosive Volcanic ERuptions (EVER). In previous simulations within the MESSy framework 3D mixing ratio perturbations of SO_2 were added manually to existing mixing ratios at fixed points in time (e. g. Schallock et al., 2023; Brühl et al., 2018). This required a high manual effort, and thus stratospheric volcanic eruptions were not part of standard simulations. The new submodel along with a newly developed historic default namelist setup for stratospheric volcanic eruptions from 1990 to 2023 (based on the emission inventory from Schallock et al. (2023) and Brühl et al. (2018)) is presented in Sect. 2.

Using the new EVER submodel, we perform three numerical experiments:

1. First, we investigate the initial SO_2 injection parameters, such as emission altitude, geographical location, emitted mass and vertical extent, with sensitivity simulations varying the aforementioned parameters. The resulting short- to mid-term SO_2 plume development is compared to satellite observations of SO_2 columns and stratospheric mixing ratios for the Nabro eruption in 2011 to tackle uncertainties in the initial stratospheric SO_2 burden introduced by the different emission inventories. We provide recommendations regarding the implementation of stratospheric SO_2 injections from volcanic eruptions within the MESSy framework (applied in the historic default namelist setup for EVER), as well as in atmospheric models more broadly.

2. Second, we evalaute a historic default namelist setup for the EVER submodel for the period from 2008-2011. This setup is developed based on the emission database from Schallock et al. (2023), and refined using observations from the IASI satellite (Clarisse et al., 2012, 2014) and the findings from our sensitivity studies. Simulated stratospheric SO_2 burden and the optical properties of the resulting stratospheric aerosol are compared to satellite observations.

3. Third, we evaluate the EVER submodel with regard to the additional use case of tropospheric degassing volcanoes with SO_2 column observations of the Kilauea degassing event from June 2018. We use SO_2 emission rates from a previous study, and provide a method to tune the emission rates, such that observed SO_2 column amounts can be reproduced.

The methods and the experimental setup is outlined in Sect. 3, and the results of the numerical experiments are presented in Sect. 4.

2 New MESSy submodel for Explosive Volcanic ERuptions (EVER)

The new submodel EVER is developed as an extension to the second version of MESSy (version 2.55.1, Jöckel et al., 2010), which can be coupled with various basemodels, i. e. General Circulation Models (GCM). MESSy employs strict coding structures across its submodels to ensure portability and high flexibility in chemistry-climate simulations.

2.1 Submodel description

The core of EVER is based on the MESSy submodel TREXP (Jöckel et al., 2010), primarily employed for artificial tracer studies and capable of emitting point sources and uniformly distributed columns of trace gases. To enable the simulation of

volcanic eruptions, novel functionalities were introduced as part of the new EVER submodel, including the incorporation of different types of vertical distributions, primary emission of aerosol species, and seamless coupling with aerosol submodels.

Volcanic eruptions or other local atmospheric emission sources can be simulated and controlled via namelist. Each volcanic eruption or emission is initiated using the following parameters:

- Geographical location (latitude and longitude)
- Type of vertical distribution (see Sect. 2.1.2)
- Altitude range (minimum to maximum altitude) [km above surface level (asl)]
- Midpoint [km asl] and sigma [km] of the eruption plume (only needed for Gaussian vertical distributions)
- Period of the (volcanic) emission (date and time of start and end)
- List of emitted tracers (corresponding to tracer names)
- List of tracer masses (in Tg)
- List of aerosol parameter sets (see Sect. 2.1.1)

Tendencies for several tracers can be estimated with one emission. Emitted tracer masses are converted to mass mixing ratio tendencies per second, that are incrementally added to the total mixing ratios during runtime, uniformly distributed over the specified time range, within the grid-column over the defined location, and following a user-specified vertical distribution. Aerosol parameter sets only need to be provided for aerosol species, and are defined as described in Sect. 2.1.1. An example Fortran95 namelist setup for the EVER submodel is provided in the supplement (ever_example.nml), in which both SO_2 and volcanic ash are emitted using the same vertical distribution and time frame. If the temporal or spatial extents differ, new emission points must be defined accordingly.

2.1.1 Primary aerosol emissions

MESSy offers several submodels for numerically simulating atmospheric aerosols. The new EVER submodel is currently designed to flexibly interface with modal aerosol submodels to emit primary aerosol, and was tested for the three MESSy aerosol submodels GMXe (Pringle et al., 2010), MADE3 (Kaiser et al., 2014, 2019) and PTRAC (Jöckel et al., 2008), while future coupling to sectional aerosol models is possible with adjustments to the interface. However, currently MESSy does not contain any sectional aerosol submodel. While PTRAC only requires an increase of the mixing ratio of the tracer for primary aerosol emissions (as diameter and density of each aerosol tracer remain fixed), the submodels GMXe and MADE3 require an additional increase in number concentration of the corresponding aerosol size mode. For these two submodels, the respective channel name ("aermod_channel" in namelist, see supplement) has to be provided.

The emitted number concentration is calculated based on aerosol parameter sets, which can be defined via Fortran95 namelist using the following variables:

- Aerosol parameter set name (referenced by the volcanic eruption points)
- Density of the emitted aerosols ρ
- Median emission particle diameter of the emitted species d_{md} [m]
- Size mode as defined in the aerosol submodel

The median emission particle diameter should reside within the diameter boundaries of the corresponding aerosol mode to ensure proper treatment of the emission. The sigma of the log-normal distribution (σ_{ln}) is obtained from the defined aerosol submodel for the given size mode. In EVER v1.0, which is included in the latest MESSy releases 2.55.1 and 2.55.2, primary emissions were handled differently. Specifically, EVER could only be directly integrated with GMXe, requiring the GMXe mode as a string, while sigma had to be explicitly provided for other submodels. The improved coupling with aerosol submodels was introduced in EVER v1.1 and will be available in all subsequent releases.

On the basis of the aerosol parameter sets, number concentrations are calculated using

$$N_{aer} = \frac{6 \cdot M_{trac}}{\pi \cdot \rho \cdot \exp\left(3 \ln d_{md} + 4.5 \ln^2 \sigma_{ln}\right)} \tag{1}$$

where M_{trac} denotes the mass of the emitted species and ρ, d_{md} and σ_{ln} as described above.

2.1.2 Vertical distributions

As volcanic plumes typically span a range of altitudes rather than being centered at a specific altitude, it is reasonable to specify vertical distributions as well for the corresponding emissions. Presently, two types of vertical distributions are supported, with the potential for expansion in the future:

1. **Uniform distribution:** In this distribution, the mass is uniformly distributed between the minimum and maximum altitudes, proportionally to the height of the grid cell. The lowermost and uppermost grid cells within the altitude range are filled based on the fraction of the grid cell covered by the altitude range.

2. **Gaussian distribution:** In this distribution, the mass follows a Gaussian-shaped vertical profile with mean altitude and sigma defined in the namelist emission entry. It can be confined to a vertical extent as for the **Uniform distribution**, truncating the tail and scaling accordingly. The emission amount in each grid cell is calculated by considering the fraction of the error function integrated from the bottom to the top of the grid cell (for the lowermost and uppermost grid cells, the minimum and maximum altitudes are used, respectively) relative to the integral of the error function across the entire confined vertical extent.

Although each injection is realized within a single column of grid boxes horizontally, multiple emission points can be defined to accurately reproduce the observed horizontal extent of a single eruption. This is especially important for large volcanic plumes entering the stratosphere, exceeding the area of one grid box (Schallock et al., 2023). Tilmes et al. (2023) showed, that the emission of the Pinatubo SO_2 plume over a horizontal area, rather than in one single column, leads to a significantly improved agreement with observations. However, in this study we only used one emission point for each eruption.

2.2 Historic default namelist setup

A primary aim of this study is the development of a methodology, that automatically integrates volcanic eruptions significantly impacting the stratosphere in standard simulations using the MESSy framework, and thus reproduces stratospheric SO_2 mixing ratios. Therefore, we established a default namelist configuration for the EVER submodel spanning the period from 1990 to 2023. This setup encompasses about 800 significant explosive volcanic eruptions, based on the SO_2 emission inventory developed by Schallock et al. (2023), which we extended up to the end of 2023, and refined with observations from the IASI satellite.

The emission inventory from Schallock et al. (2023) provides information regarding the mass of emitted SO_2 reaching the stratosphere, the plume altitude as observed from satellites, the initial satellite observation date, and the geographic coordinates of the volcano. This inventory was translated into an EVER namelist. The development of the emission inventory involved satellite observations and information from the Global Volcanism Program, Smithsonian Institute (https://volcano.si.edu/, last access: 25 March 2024). It is important to note that this inventory may not include all relevant volcanic events, and we encourage the community to contribute additional significant volcanic events to the extendable namelist.

The emission inventory is refined using IASI observations as follows: For each volcano, we conduct a scan of both, temporal and spatial parameters, extending ± 10 days from the emission inventory date and $\pm 10^\circ$ latitude and $\pm 15^\circ$ longitude from the volcano's geographical coordinates. From this analysis, we extract the space-time point exhibiting the maximum stratospheric SO_2 mixing ratios observed by IASI as the optimal estimate for both, timing and geographical location for injecting the plume into the stratosphere.

The SO_2 mass is then distributed vertically in a Gaussian profile centered 1 km below the maximum altitude (sigma of 2 km, confined to the vertical extent of the maximum plume altitude down 2 km, truncating the Gaussian distribution at $\sigma/2$) recorded in the emission inventory, over 6 hours around the identified date and time of peak mixing ratio as default. In reality, eruption duration and plume vertical extent may vary, and can be adjusted for the study of specific eruptions. It is important to note that IASI became operational only in 2007 and primarily observes larger volcanoes. For eruptions occurring before 2007 or those not observed, we utilize the geographical location of the volcano and release the SO_2 mass from 9:00 to 15:00 UTC on the date provided by the emission inventory from Schallock et al. (2023). Consequently, these emissions are subject to uncertainties as discussed later.

We provide the namelist setup as supplement (ever_historic_stratVolcanoes.nml) for direct application in numerical simulations with the EVER submodel. All injections optimized using the IASI observations are marked accordingly.

3 Methods

3.1 Observations

SO_2 and optical properties of aerosols in the atmosphere are continuously monitored by satellites. We use satellite observations of volcanic plumes for the evaluation of the new submodel, shortly summarized in Table 1. More details can be found in the

Table 1. Summary of satellite instruments and the respective observed quantities used for the evaluation of model simulations with the EVER submodel. More technical details in the observations and the applied retrievals can be found in the provided references.

Instrument & Satellite	Observation method	Retrieved quant.	Operation	Reference
Infrared Atmospheric Sounding Interferometer (**IASI**) – MetOp	Thermal infrared emission from Earth (nadir)	$\mathbf{SO_2}$ – columm + altitude retrieval	2006–now	Clarisse et al. (2012, 2014)
Ozone Monitoring Instrument (**OMI**) – Aura	UV & vis. solar backscatter radiation from Earth's surface (nadir)	$\mathbf{SO_2}$ – total column	2004–now	Li et al. (2020)
Michelson Interferometer for Passive Atmospheric Sounding (**MIPAS**) – ENVISAT	Mid-infrared emission spectrometer (limb)	$\mathbf{SO_2}$ – 3D (stratosphere)	2002–2012	Höpfner et al. (2013, 2015)
TROPOspheric Monitoring Instrument (**TROPOMI**) – Sentinel-5P	As OMI, extended to UV, visible, near-IR & shortwave	$\mathbf{SO_2}$ – column (troposphere)	2017–now	Theys et al. (2017)
Optical, Spectroscopic and Infrared Remote Imaging System (**OSIRIS**) – ODIN	Spectrally dispersed, scattered sunlight (limb)	**Aerosol extinction** at 750 nm – 3D (strat.)	2001–now	Rieger et al. (2019)

provided references. Section 3.2 outlines which observations were used for which study. The versions of the used datasets are provided in the data availability section.

Satellites typically do not directly observe the retrieved variables but rather functions of these variables, which rely on certain a priori information (Rodgers and Connor, 2003; Rodgers, 1990; Raspollini et al., 2006). Additionally, observed values are influenced by the horizontal and vertical resolutions used for retrieval, leading to contributions from neighboring layers. To account for this effect, averaging kernel matrices (AKM) can be applied to model data for comparison purposes. In this analysis, AKMs are used for comparisons with MIPAS observations. It is important to note that it is not possible to invert the AKM to correct the retrieved product.

3.2 Model setup and numerical experiments

We perform three separate numerical model experiments for the evaluation of the new submodel EVER and the established historic namelist setup. All simulations are performed with the ECHAM5/MESSy Atmospheric Chemistry (EMAC) model (Jöckel et al., 2006) that couples MESSy2 (Jöckel et al., 2010) to the general circulation model ECHAM5 (version 5.3.02, Roeckner et al., 2003). Temperature, the logarithm of the surface pressure, divergence and vorticity are "nudged" (more details by Jöckel et al., 2006; Jeuken et al., 1996) towards meteorological reanalysis data (ERA5, Hersbach et al., 2020) from the European Centre for Medium-Range weather forecasts (ECMWF) below 100 hPa. In addition, we employ the QBO submodel to weakly nudge the simulations to QBO zonal wind observations between 10 and 90 hPa (Giorgetta et al., 2002) to avoid a phase drift.

Gas-phase chemistry is addressed by the MECCA submodel (Sander et al., 2019). Details on the selected chemical mechanism in the different experiments are given below. Emissions from anthropogenic and biogenic sources, and from biomass

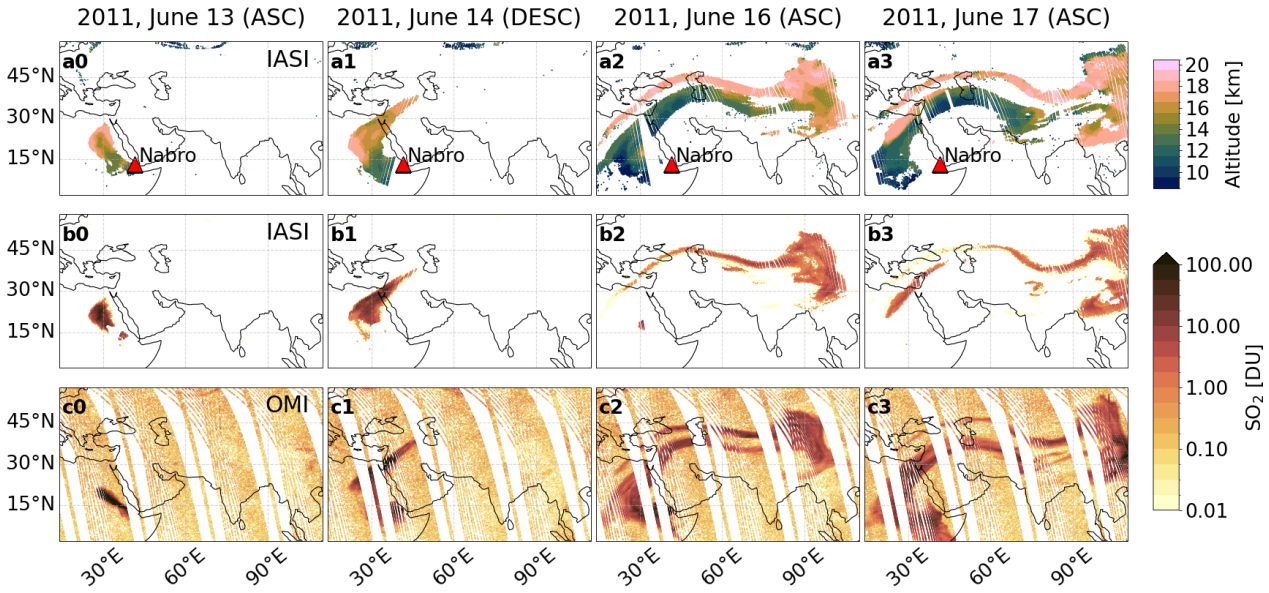

Figure 1. Observations of the Nabro plume on selected dates in the first week after the Nabro eruption. **a***, SO_2 plume height retrievals from IASI satellite observations (Clarisse et al., 2014) during ascending (ASC) and descending (DESC) orbits **b*,** Derived SO_2 columns from IASI (Clarisse et al., 2014) observations. **c*,** Derived SO_2 columns from OMI (Li et al., 2020) observations. IASI SO_2 columns are calculated assuming that all SO_2 is centered at the retrieved plume height (top row), and we only display pixels where the retrieved SO_2 plume is detected in the stratosphere (above 14 km), whereas OMI displays the total column. Note that the timing of the observations does not coincide in general.

burning are introduced as described by Kohl et al. (2023). Sedimentation, dry and wet deposition are simulated using the submodels SEDI, DDEP (both Kerkweg et al., 2006), and SCAV (Tost et al., 2006), respectively. Namelist setup, chemical mechanism and runscript for the stratospheric (Sect. 4.1 & 4.2) and the Kilauea (Sect. 4.3) simulation can be found in the supplement.

3.2.1 SO_2 in explosive volcanic eruptions — Nabro (2011)

First, we evaluate the EVER submodel and investigate the sensitivity of the resulting SO_2 plume to the injection parameters with the eruption of the Nabro volcano, starting on 13 June 2011 (Global Volcanism Program, 2011). The volcanic cloud predominantly comprised water and SO_2, reaching up to 20 km in altitude. As it was observed by a number of satellite instruments in contrast to the stronger eruption of Mount Pinatubo, it offers a perfect case study to investigate the spatio-temporal evolution of volcanic SO_2 in the stratosphere.

Figure 1 illustrates the evolution of the plume during the first days after the initial eruption, as observed from IASI and OMI. The top panel provides SO_2 height retrievals from IASI (Clarisse et al., 2014). The second and third row show retrieved

SO_2 columns from IASI and OMI, respectively. SO_2 columns derived from IASI are presented only for coordinates where the retrieved SO_2 height exceeds 14 km, whereas OMI observes the total column. It is noteworthy that the precise timing of the satellite overpasses does not align for IASI and OMI observations.

The initial stratospheric plume followed a northwestward trajectory during its ascent, entering the stratosphere at approximately $18°N$, $30°$ E, and an altitude of up to 18 km (see Fig. 1 a-c0). Within the UTLS, the SO_2 plume is influenced by the Asian Monsoon Anticyclone, subsequently evolving in a northeastward direction (Fig. 1 a-c1). In the night of June 15 to June 16, an additional plume entered the stratosphere, as evident in the IASI observations from June 16 (Fig. 1 a2). Concurrently, a wind shear within the AMA around the tropical tropopause induced a separation between tropospheric and stratospheric SO_2, with the stratospheric component further north (Fig. 1 a2,3). Subsequently, the SO_2 originating from the stratospheric entries mixed and was transported in the anticyclone. Approximately 10 days after the initial eruption, stratospheric SO_2 was distributed widely across the displayed region (not shown).

The difference between the stratospheric IASI SO_2 observations and OMI total columns confirms the altitude-specific findings depicted in the top panel of Fig. 1, enabling a distinction between tropospheric and stratospheric contributions to the total column. Furthermore, it highlights that while the Nabro volcano continuously emitted, plumes entered the stratosphere exclusively on June 13 and June 16. It is debated, if these stratospheric entries resulted from a direct injection caused by the eruption, or if the initial plumes failed to reach the stratosphere, subsequently being uplifted within the South Asian monsoon system (Bourassa et al., 2012; Fromm et al., 2013; Vernier et al., 2013; Bourassa et al., 2013; Clarisse et al., 2014). Especially the second stratospheric plume on June 16 could comprise remnants of the tropospheric plume from June 13, that are uplifted. This study does not engage in this ongoing discussion, but exclusively concentrates on the stratospheric entrance points of the plume.

To comprehensively evaluate volcanic SO_2 emissions with the EVER submodel and explore the impact of simplifications and adjustments to emission data, we conducted a reference simulation along with a series of sensitivity simulations of stratospheric SO_2 of the Nabro eruption. We applied a horizontal resolution of T63 (approx. 190×190 km at the equator), 90 vertical levels up to 0.01 hPa and a model timestep of 8 minutes. The SO_2 injection parameters of the reference simulation are based on the emission inventory developed by Schallock et al. (2023), refined with IASI obserations (see below). We employed the Mainz Isoprene Mechanism (MIM1; Pöschl et al., 2000; Jöckel et al., 2006) within MECCA (see supplement for detailed mechanism), considering oxidation of SO_2 with OH to form SO_3, subsequently reacting with H_2O to form H_2SO_4. Carbonyl sulfide (OCS), a precursor for stratospheric aerosols, is constrained using monthly averaged surface concentrations as outlined by Montzka et al. (2007). Dimethyl sulfide (DMS) emissions from the ocean are computed using the MESSy submodel AIRSEA (Pozzer et al., 2006) and global ocean surface DMS concentrations derived by Lana et al. (2011) in the stratospheric setup.

The following simulations were performed:

- **reference**: Column emission centred at altitude from the emission inventory minus 1 km (17 km); Gaussian vertical distribution with a sigma of 2 km, confined to the altitude range from 16 to 18 km (see Sect. 2.1.2); horizontal position and timing derived from IASI (one column encompassing 22.9°N, 29.7°E on June 13, 2011, 16:00 - 22:00 UTC); SO_2 amount (406 kt) from the emission inventory from Schallock et al. (2023).

- **optimized**: Same as **reference**, but with the total amount distributed on two stratospheric entry points (67% on June 13 and 33% on June 16 based on the qualitative findings from the IASI observations).
- **reduced**: Same as **reference**, but with reduced SO_2 emissions (280 kt).
- **volc_pos**: Same as **reference**, but emissions injected at the geographical location of the volcano (13°N, 41°E).
- **point**: Same as **reference**, but using only one single grid-box at the emission inventory altitude minus 1 km (17 km).
- **min_2days**: Same as **reference**, but emissions shifted by two days (June 11, 2011, 16:00 - 22:00 UTC).
- **plus_1km**: Same as **reference**, but emissions shifted by 1 km in altitude (18 km).
- **mills_et_al**: Emissions as described by Mills et al. (2016). The emissions are injected over several days and in columns covering the free troposphere and the UTLS region, ranging from 2.5 to 17 km. The only partly stratospheric emission takes place on June 13, emitting 1500 kt, uniformly distributed over the altitude range from 9.7 to 17 km.

For the short-term evaluation (first week after the initial eruption) of the simulations we use IASI observations, as they provide detailed information on the short-term SO_2 plume evolution (Sect. 4.1.1). SO_2 columns are sampled at the time of the satellite's overpass for comparison with the IASI satellite using the SORBIT submodel (Jöckel et al., 2010).

However, IASI faces limitations in capturing the mid-term evolution of volcanic plumes with SO_2 columns falling below the instrument's detection limit. This can likely be attributed to the dilution and chemical removal of the volcanic SO_2. Conversely, observations from the MIPAS instrument are not well-suited for short-term analysis as observed mixing ratios only slowly build up after strong volcanic eruptions. Höpfner et al. (2015) provide two main reasons for this behavior. First, the enhanced concentration of volcanic particles in the plume may lead to the exclusion of the retrieved spectra, and thus non-plume air masses are favored. Second, the enhanced SO_2 mixing ratios saturate the spectral lines. Indeed, MIPAS observations become more reliable approximately three weeks after the initial eruption. Its ability to provide three-dimensional SO_2 observations makes it well-suited for the mid-term monitoring of SO_2 plumes (Sect. 4.1.2).

For the comparison with MIPAS observations, we calculate the stratospheric SO_2 burden. As the model tropopause does not necessarily coincide with the observed tropopause, we apply fixed lower integration limits for the calculation of the stratospheric SO_2 burden, depending on latitude (16 km for 0-30°, 14 km for 30-60° and 12 km for 60-90°). We investigate the sensitivity of the model-observation agreement to the lower integration limit in Appendix A, showing changes in absolute values at similar agreement when varying the lower integration limit, thus justifying the usage of fixed lower integration limits for the evaluation.

3.2.2 Multi-year simulation with the historic namelist setup

Second, we performed a numerical simulation spanning from January 2008 to December 2011 to evaluate the newly developed historic volcanic setup for the EVER submodel (see Sect. 2.2), using the same model configuration as detailed in Sect. 3.2.1. This timeframe is characterized by high volcanic activity, including three strong eruptions — Kasatochi (August 2008),

Sarychev (June 2009) and Nabro (June 2011) — alongside several smaller eruptions. Over the simulated four years, a total of 107 stratospheric injections from volcanic events are documented by Schallock et al. (2023) and considered in the simulation.

We use 3-dimensional observations from the MIPAS instrument to evaluate the total stratospheric SO_2 burden (Sect. 4.2.1) with the same lower integration limit as described above. To additionally validate the simulation, we evaluate the extinction and sAOD at 750 nm of the resulting stratospheric aerosol with observations from the OSIRIS instrument in the tropics (0-25°N, lower integration limit 16 km) and at higher northern latitudes (45-80°N, lower integration limit 12 km), as the tropopause altitude is fairly constant in these regions (Sect. 4.2.2).

Aerosol microphysics are treated with the submodel GMXe (Pringle et al., 2010). In our simulations, we apply four hydrophilic modes (Nucleation, Aitken, Accumulation, and Coarse) and three hydrophobic modes (Aitken, Accumulation, and Coarse). We use the same GMXe setup as detailed in Schallock et al. (2023). Inorganic aerosol thermodynamics are treated with ISORROPIA-II (Fountoukis and Nenes, 2007), and sulfuric acid-water nucleation follows the parameterization by Vehkamäki et al. (2002). We calculate simulated AERosol OPTical properties of the GMXe aerosol populations with the AEROPT submodel (Dietmüller et al., 2016), providing extinction coefficients and aerosol optical thickness of each model layer at various wavelengths.

The additional evaluation of the simulated aerosol optical properties shall not evaluate the model's microphysics described above, but serve as an additional validation of the approach with OSIRIS observations, and a comparison to the simulation done by Schallock et al. (2023), who used a similar setup.

3.2.3 SO_2 from degassing volcanoes — Kilauea (2018)

Third, we evaluate the submodel's capability to simulate degassing volcanoes by analyzing the emissions following a series of eruptive fissures at the Kilauea volcano in Hawaii, USA, in summer 2018 (Kern et al., 2020). SO_2 emissions from Kilauea were studied with the EMAC model before for a different period (Beirle et al., 2014).

Simulations are performed at a horizontal resolution of T255 (approximately 50×50 km at the equator) and 31 model levels (up to an altitude of about 30 km) to capture the tropospheric transport. The timestep has to be decreased to 2.5 minutes to account for the increased horizontal resolution. We use a simplified chemistry covering the basic tropospheric chemistry, including O_3, OH, NOx, NOy and basic sulfur chemistry (see supplement for details). Oxidation of SO_2 to H_2SO_4 is directly realized via reaction with OH, without producing any intermediates. We do not consider DMS and OCS here (see supplement), leading to a potential underestimation of background maritime SO_2 concentrations.

The Kilauea SO_2 emissions are clearly observed from TROPOMI (ESA, 2018), serving as a basis for comparison with simulated columns. Jost (2021) derived daily SO_2 emission rates for Kilauea based on TROPOMI observations (SO2 repro v1.1) and wind fields from ECMWF, using the divergence method developed by Beirle et al. (2019). Within this study, we use the original emission rates scaled up by a factor of 4.3 following recent updates, resulting in higher emission estimates. These adjustments include:

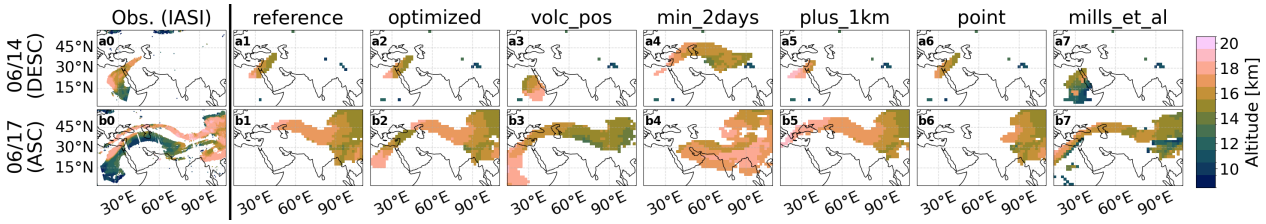

Figure 2. Derived plume altitude from the IASI satellite observations (left; compare Fig. 1) is compared with the altitude of maximum SO_2 mixing ratios for each vertical column from the sensitivity simulations, one day (top) and four days (bottom) after the initial Nabro eruption. In the simulations SO_2 was only injected into the stratosphere, except for **mills_et_al**.

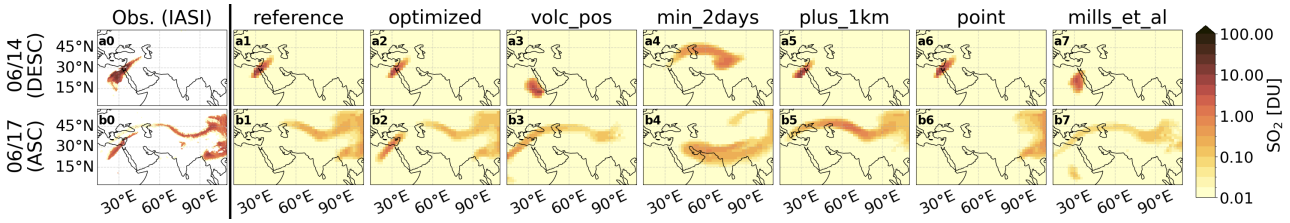

Figure 3. Column SO_2 derived from IASI satellite observations (left; compare Fig. 1) is compared with the respective column from the sensitivity simulations, one day (top) and four days (bottom) after the initial Nabro eruption. In the simulations SO_2 was only injected into the stratosphere, except for **mills_et_al**.

(a) A factor of 3.2 due to non-linear effects caused by strong SO_2 absorption in the Kilauea volcanic plume (compare Theys et al., 2017). While Jost (2021) initially deemed this effect negligible, we included it after re-examination.

(b) A factor of 1.12 due to the change of the assumed plume height from 2000 m to 1000 m (compare Kern et al., 2020).

(c) A factor of 1.19 from the consideration of topographic effects on the divergence calculation (Sun, 2022; Beirle et al., 2023).

In addition, we perform a simulation with tuned emission rates. For that purpose, we first fit the emission rates from Jost (2021) to the resulting simulated SO_2 columns. Subsequently, we optimize the model's emission rates gradually by using a stochastic gradient descent algorithm (e. g. Ruder, 2016) to match the observed columns. More details on the optimization can be found in Appendix B.

4 Evaluation & Results

4.1 SO_2 in explosive volcanic eruptions — Nabro (2011)

4.1.1 Short-term SO_2 plume evolution

Figures 2 and 3 compare the simulated altitude of maximum SO_2 mixing ratios and SO_2 columns from the reference and sensitivity simulations to the corresponding IASI observations for the morning overpass on June 14 (one day after the initial Nabro eruption) and the afternoon overpass on June 17. SO_2 emissions in the simulation are confined to the stratosphere (except the approach by Mills et al. (2016)), and thus only stratospheric amounts (altitude $\geq$ 14 km) are shown. Indeed, this approach neglects the significant amount of tropospheric SO_2 injected during the eruption. However, tropospheric SO_2 typically has a much shorter lifetime compared to stratospheric SO_2, which we focus on in this study. The **reduced** simulation is not shown in these figures, as it is equivalent to the **reference** in altitude and only exhibits reduced columns.

Overall, the simulated columns appear to be underestimated when compared to observations (see Fig. 3b*). However, this might be attributed to the retrieval procedure of the column from the IASI observations. The column estimation assumes that all SO_2 of the plume is centered at the respective altitude depicted in Fig. 2. However, it takes into account the complete column, also including the tropospheric part of the plume. Hence, we only conduct a qualitative comparison between the simulated and observed column.

The **reference** simulation appears to reasonably capture the stratospheric evolution when considering only pixels where the altitude exceeds 14 km, although some discrepancies are evident. While the simulated altitude distribution horizontally broadens over time (Fig. 2 b1), the total column analysis (Fig. 3, June 17 **reference**) shows that the columns at the edges of the plume are very low, falling below the detection limit of IASI. Notably, as the **reference** simulation assumes only one stratospheric entrance, it fails to reproduce the observed second plume as expected (compare Fig. 3 b0 and b1).

In the **optimized** simulation the emissions are distributed across two space-time points, based on a detailed analysis of the IASI observations (refer to Fig. 1). As a result, the second plume is successfully reproduced, leading to better agreement with the observations (Fig. 3 b2). By varying the geographical location of the stratospheric entrance (**volc_pos**), the plume encounters different meteorological patterns, resulting in a distinct evolution pattern. Similarly, adjusting the timing parameter (**min_2days**) leads to a more advanced evolution within the anticyclone (Fig. 3 b4). These sensitivity analyses highlight the importance of accurately representing the timing and location of stratospheric injections for capturing the short-term evolution of volcanic plumes in atmospheric models.

As previously mentioned, a vertical wind shear leads to a displacement of the stratospheric part of the plume towards higher latitudes. Moreover, there appears to be a vertical gradient in wind speed above 16 km. When the emission altitude is increased by 1 km (**plus_1km**), the evolution within the anticyclone is attenuated (Fig. 2 b5), suggesting lower wind speeds at higher altitudes. Additionally, the **point** simulation, where all emissions are centered at 17 km, only reproduces the rapid branch of the observed plume evolution. Consequently, it does not encounter the lower wind speeds experienced at higher altitudes (Fig. 2 b6). In contrast, Mills et al. (2016) implemented emissions over several days and uniformly over altitudes ranging from 2.5

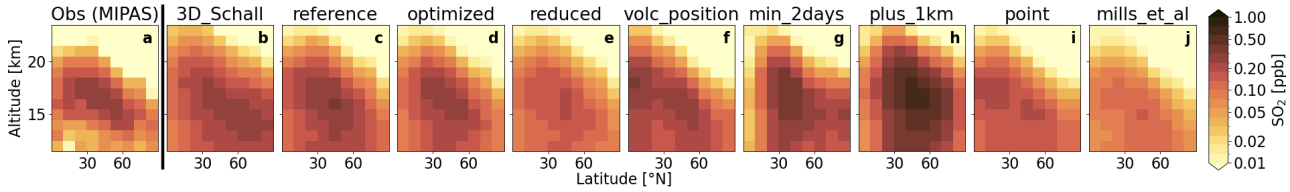

Figure 4. Zonally and 5-day averaged (July 14 - July 18, 2011) profile of northern hemispheric stratospheric SO_2 mixing ratios derived from MIPAS observations (leftmost panel) is compared with the respective SO_2 mixing ratios simulated in the reference and sensitivity simulations one month after the eruption of the Nabro volcano.

to 17 km, accounting for the continuous emissions that did not reach the stratosphere. However, in the **mills_et_al** simulation, stratospheric emissions are underestimated, leading to a substantial fraction of emissions being lost due to scavenging in the free and upper troposphere (Fig. 2 b6).

4.1.2 Mid-term SO_2 mixing ratios

The zonal and 5-day averaged profiles of simulated and observed (MIPAS) stratospheric SO_2 mixing ratios on July 16, 2011, approximately one month after the eruption, are shown in Figure 4 for the Northern Hemisphere. In addition to the sensitivity simulations discussed earlier, a simulation using 3D emission fields of SO_2 mixing ratios (**3D_Schall** in the following) is included for comparison (Schallock et al., 2023). These emission fields were derived from various satellite observations and applied several days after the initial eruption, specifically on June 21 for the Nabro eruption. Details on the methodology are described by Schallock et al. (2023). To simulate the effect of limited vertical resolution associated with MIPAS observations, the AKM (see Sect. 3.1) was applied to all simulated SO_2 mixing ratios.

The comparison between simulated and observed SO_2 distributions reveals some discrepancies, particularly in the vertical extent of the elevated SO_2 mixing ratios. The SO_2 distributions exhibit a slightly larger vertical extent compared to the observations. This discrepancy suggests a potential overestimation of the AKM or limitations in the vertical resolution of the simulation at the respective altitudes (approximately 500 meters). Interestingly, the **3D_Schall** simulation, which uses 3D emissions derived directly from satellite observations, shows the widest distribution (b). This discrepancy can be attributed to the fact that the 3D emissions already incorporate the smoothing effects introduced during the retrieval process (i. e. the AKM). Consequently, the simulated SO_2 mixing ratios in the **3D_Schall** simulation represent observed mixing ratios rather than actual mixing ratios. Therefore, after applying the AKM to these simulated mixing ratios, the resulting altitude resolution appears too wide.

The sensitivity studies exhibit consistent patterns, with the highest mixing ratios of SO_2 typically observed between 15 and 20 km in altitude and 20° and 60° N in latitude, and decreasing altitudes of highest SO_2 mixing ratios with increasing latitude. The distribution follows the typical stratospheric circulation pattern and resembles the observed distribution. Lower mixing ratios compared to observations are found in the **reduced**, **point**, and **mills_et_al** simulations. In the **reduced** simulation, the reduced emissions directly lead to lower mixing ratios (e). However, in the **mills_et_al** simulation, a significant

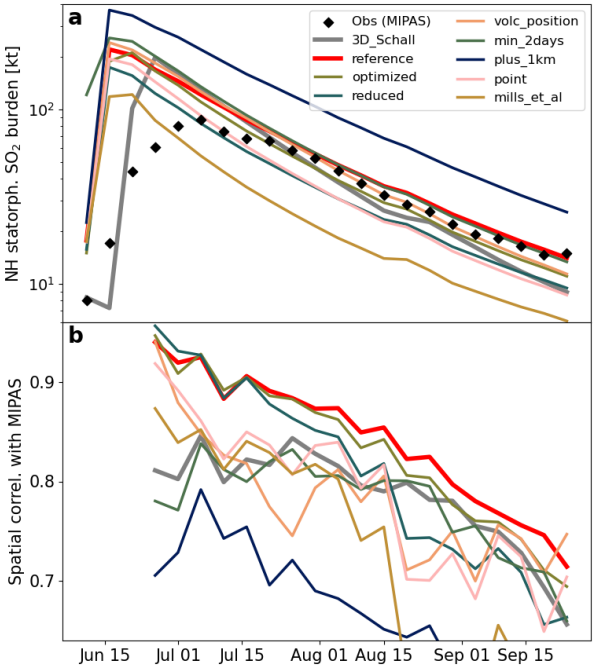

Figure 5. The top panel displays the total northern hemispheric (NH) stratospheric SO_2 burden as observed from the MIPAS satellite (black dots) and from the sensitivity simulations (5-day averages). In the bottom panel, we depict the spatial correlation in the latitude-altitude plane between the simulations and MIPAS observations, i. e. the spatial correlation between the first and all other panels in Fig. 4.

portion of SO_2 is removed in the upper troposphere, as discussed earlier (j). In the **point** simulation, restricting emissions to a single grid box omits the altitude range between 17 and 18 km, leading to a reduced stratospheric lifetime (i). Conversely, the **plus_1km** simulation shows higher mixing ratios due to the increased stratospheric lifetime associated with higher injection altitudes. Interestingly, the **volc_pos** (f) and **min_2days** (g) simulations exhibit slightly different spatial distributions, with the former indicating higher and the latter lower SO_2 mixing ratios at low latitudes. Hence, the varied meteorological conditions experienced in the initial days post-eruption consistently lead to diverse mid-term evolutions of stratospheric SO_2.

In addition to examining the spatial distributions at specific time points, we explored the mid-term changes of northern hemispheric (NH) stratospheric SO_2 burden (Fig. 5a) and the mid-term spatial agreement between observed and simulated SO_2 mixing ratios (Fig. 5b) after the Nabro eruption. MIPAS observations of NH stratospheric SO_2 burden exhibit a gradual increase following the volcanic eruption, unlike the simulations, as discussed earlier. The **3D_Schall** simulation's onset is delayed by a week, as the simulation is based on observations after the first plume evolution in the stratosphere. The bottom panel of Fig. 5 illustrates the spatial correlation between the zonal profile of MIPAS observations and the sensitivity studies within the altitude-latitude window depicted in Fig. 4.

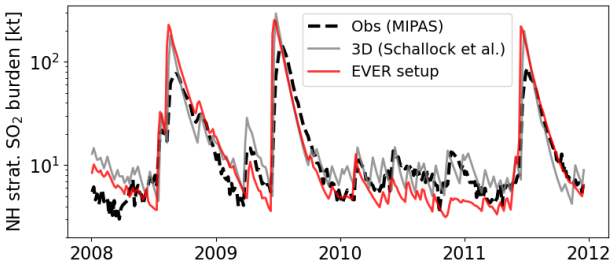

Figure 6. Timeline of total northern hemispheric (NH) stratospheric SO_2 mass as observed from the MIPAS instrument (black dashed line) compared with simulations using the EMAC model with the new EVER historic volcanic setup (red) and using 3D emission fields (Schallock et al., 2023).

The stratospheric SO_2 burden of the **reference**, **optimized**, **volc_pos** and **min_2days** simulations follow the same logarithmic decay, mostly coinciding with the observations after mid-July. These simulations also exhibit very similar spatial correlations with some fluctuations, showing correlations around 0.9 approximately 3 weeks after the eruptions, which gradually decrease to values between 0.75 and 0.8 in late September. The **min_2days** simulation shows a weaker correlation in the initial phase but approaches the others in the mid-term, most likely due to the different initial meteorological conditions.

The **reduced**, **point** and **mills_et_al** simulations exhibit consistently lower stratospheric SO_2 mass as observed earlier, while the decay is parallel to the aforementioned. The spatial correlation of the **reduced** and **point** simulations is similar to the **reference** simulation, while the **mills_et_al** simulation shows a slightly smaller but comparable correlation. Emissions at higher altitudes (**plus_1km**) lead to higher SO_2 burden, longer lifetime, and lower spatial correlation with the observations. Initially, the simulation with three-dimensional emissions (**3D_Schall**) shows a comparable total stratospheric SO_2 burden to the reference simulation. However, it displays a slightly shorter lifetime as the burden decays more rapidly. Additionally, a slightly lower spatial correlation is observed, potentially attributed to the wider distribution of emissions.

The overall slightly faster decline of the stratospheric SO_2 burden in the simulation compared to the observations appears consistent across all simulations. It can either be attributed to an overestimation of the chemical removal, i. e. the oxidation with OH, or too efficient transport from the stratosphere to the troposphere, that also depends on the injection altitude and to a lesser extent the injection location.

4.2 Evaluation of the historic default namelist setup in a multi-year simulation from 2008 to 2011

4.2.1 Stratospheric SO_2 burden

Figure 6 illustrates total NH stratospheric SO_2 burdens, analogously to the upper panel of Fig. 5 for the simulated timeframe from January 2008 to December 2011. We compare our simulation using the new EVER setup to the simulation from Schallock et al. (2023) using 3D emissions and observations from MIPAS.

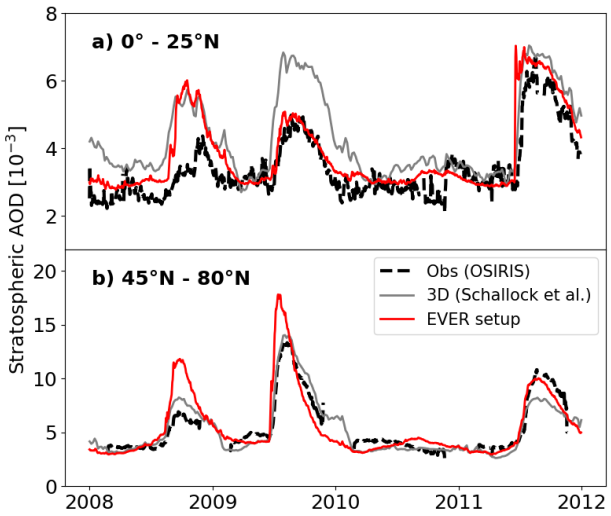

Figure 7. Timeline of sAOD at 750 nm (for the vertical range of the integration see Sect.3.2.2) as observed from the OSIRIS instrument (black dashed line) compared with simulations using the EMAC model with the new EVER historic volcanic setup (red) and with 3D emission fields (Schallock et al., 2023). The sAOD is evaluated in the northern hemispheric tropical latitudinal band from 0° to 25°N (top) and at higher northern latitudes from 45° to 80°N (bottom).

The three primary peaks are largely reproduced similarly in both simulations, as anticipated, given that the injection mass from the emission inventory is derived from the 3D emission fields in the work of Schallock et al. (2023). However, in general, the observed peaks are lower than the simulated ones. This discrepancy can be attributed to the limited reliability of MIPAS observations shortly after strong eruptions (see Sect. 3.2.1 and 4.1.2 for details), underestimating actual SO_2 mixing ratios.

The EVER simulation exhibits an underestimation of background SO_2 mixing ratios, particularly evident during the relatively quiet period from the end of 2010 until the eruption of Nabro in June 2011, whereas the 3D simulation mostly reproduces the background mixing ratios. The discrepancy in the EVER setup is likely attributable to limitations in the general model configuration or the overestimation of the vertical extent of the emissions for smaller eruptions, only reaching the tropopause. Future efforts will concentrate on enhancing the representation of background SO_2 and aerosol in both, the free and upper troposphere, as well as in the stratosphere. However, it is worth noting that the simulation does reproduce smaller volcanic events, albeit at reduced magnitudes. As previously discussed, these smaller injections are not optimized in terms of horizontal position and timing, as they fall below the detection limit of IASI.

4.2.2 Optical properties of the resulting stratospheric aerosol

So far, we focused on SO_2 in the stratosphere for the evaluation of the EVER submodel. Once in the atmosphere, the SO_2 can convert to sulfur aerosol particles, with e-folding times varying between 2 and 40 days (Carn et al., 2016; Höpfner et al., 2015).

For an additional validation and comparison to the simulation performed by Schallock et al. (2023), we compare the optical properties of the resulting stratospheric aerosol to observations from the OSIRIS instrument.

Figure 7 shows the sAOD for the four simulated years, categorized into two regions: the NH tropics ($0°$ to $25°$N) and the mid- to higher latitudes in the northern hemisphere ($45°$N to $80°$N). In both regions, the three major peaks corresponding to the volcanic eruptions are evident. Discrepancies between the EVER simulation and observations are expected in regions where the stratospheric injection occurred, attributable to cloud overlap and saturation effects in the observations. This discrepancy is observed for Kasatochi (2008) and Sarychev (2009) at higher latitudes, and for Nabro at lower latitudes. Conversely, the 3D emissions, directly derived from satellite observations and applied with a delay, reproduce these measurement biases.

In the aftermath of the Nabro eruption in June 2011, the sAOD in the EVER simulation exhibits a sharp increase followed by notable fluctuations. The fluctuations can be attributed in part to the movement of the plume center across the $25°$ latitude band, resulting in variable alignment with the observed latitude window. The fluctuations could also be a consequence of microphysical processes, that are outside of the scope of the manuscript. Notably, the observations show similar fluctuations in the following.

Another interesting feature is the pronounced overestimation of sAOD in the tropical latitudes following the Kasatochi eruption. This anomaly could be attributed to an overestimation of transport from higher latitudes to the tropical stratosphere, or a general overestimation of the emissions. Notably, this feature is not observed after the Sarychev eruption in the EVER simulation, although it is present in the 3D simulation. The discrepancies between the two simulations in the mid-term transport after the Sarychev (to the tropics) and Nabro (to high latitudes) eruptions may be attributed to the different timing of the emissions. While emission times in the EVER simulation were optimized to the first detection of stratospheric SO_2 from the IASI satellite, 3D emissions were applied on the dates specified in Schallock et al. (2023). The interaction with the South Asian monsoon anticyclone potentially causes differing transport to lower or higher latitudes, respectively, if altitude, timing and geographical location of the emission do not coincide.

Figure 8 displays the aerosol extinction at 750 nm, as observed from the OSIRIS instrument and simulated. The effect of the three major volcanic eruptions is mostly evident between 16 and 20 km in the tropics, and between 12 and 18 km at higher latitudes. Similar to Fig. 7, the magnitude of extinction is differing between the observations and the two simulations. In addition, discrepancies are noticeable in the maximum altitude of the plume and below the tropopause. While the 3D simulation largely reproduces the observed maximum altitude, using satellite observations with, in case of MIPAS, the incorporated AKM as input, the EVER simulation may present more realistic maximum altitudes. The differences between the observations and the simulation below the tropopause are strongly driven by the coincidence with clouds which hinder the retrieval of aerosol extinction. The slight differences between the two simulations from 10 to 15 km in the tropics can most likely be attributed to the differences between the simulation setups. In addition, the QBO signal with differing aerosol concentrations above 20 km, depending on the QBO phase (e. g. Hommel et al., 2015), is more pronounced in the simulation, potentially subject to future studies.

Interestingly, in the sensitivity simulations from Brodowsky et al. (2021), the emission database from Brühl et al. (2018) consistently showed the lowest stratospheric aerosol amounts compared to the other emission databases in bad agreement

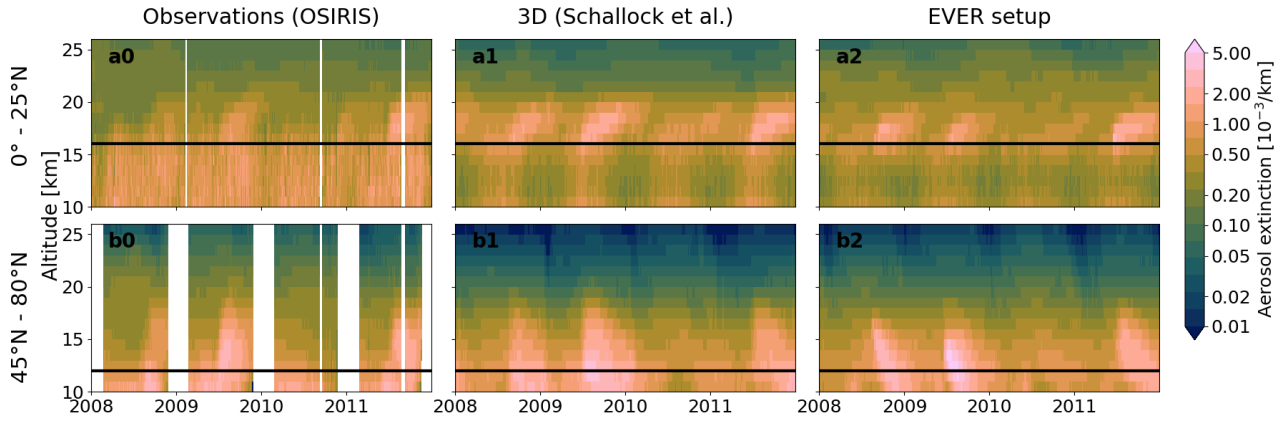

Figure 8. Timeline of aerosol extinction at 750 nm as observed from the OSIRIS instrument (left) and simulated by the EMAC model using 3D emissions (middle; Schallock et al., 2023) and using the new EVER historic volcanic setup (right), evaluated in the northern hemispheric tropical latitudinal band from 0° to 25°N (top), and at higher northern latitudes from 45° to 80°N (bottom).

with observations. However, we show much better agreement with observations in our simulations and see even higher SO_2 mixing ratios, when applying the emission inventory of Schallock et al. (2023, extension of Brühl et al. (2018)) compared to the emission database from Mills et al. (2016). This contradiction can be attributed to the vertical extent of the emission. In Brodowsky et al. (2021), "the emitted SO_2 plume is assumed to be evenly distributed [from] the given plume top downwards one third of the way to the Earth's surface", which would mean a vertical extent of 12 to 18 km for the Nabro volcano. While this approach seems reasonable for the databases of Diehl et al. (2012) and Carn et al. (2017), as they consider the tropospheric and stratospheric part of the plume, it leads to a vast underestimation of the stratospheric SO_2 when applied on the stratospheric emissions by Brühl et al. (2018). In this study, SO_2 is emitted between 16 and 18 km for the Nabro volcano in our simulations.

4.3 SO_2 from degassing volcanoes — Kilauea (2018)

Next, we want to investigate the degassing event at Kilauea. Figure 9 depicts a comparison between observed columns from TROPOMI in the top row (a*) and simulated columns from the simulations with derived emission rates from Jost (2021) (**Jost2021**, b*) and with optimized emission rates (**optimized**, c*). Generally, SO_2 columns are highest in proximity to the Kilauea volcano and disperse according to meteorological conditions. Qualitatively, we observe reasonable agreement in the horizontal dispersion of the plume on most days (Fig. 9), with some exceptions, such as June 7 and June 10. However, there is stronger variability in the observations within the transported plume compared to the simulations, where we predominantly observe gradually decreasing SO_2 columns with distance from the volcano. This effect is attributed to the diurnal variability of the SO_2 emissions, which are not represented in the emission dataset.

Figure 10 provides a quantitative assessment of the horizontal extent depicted in Figure 9 (spanning from -168° to -152° W, 15° to 25° N), showing spatially averaged SO_2 column within this horizontal window, $\overline{SO_{2(\mathrm{col},d)}}$ as observed and simulated

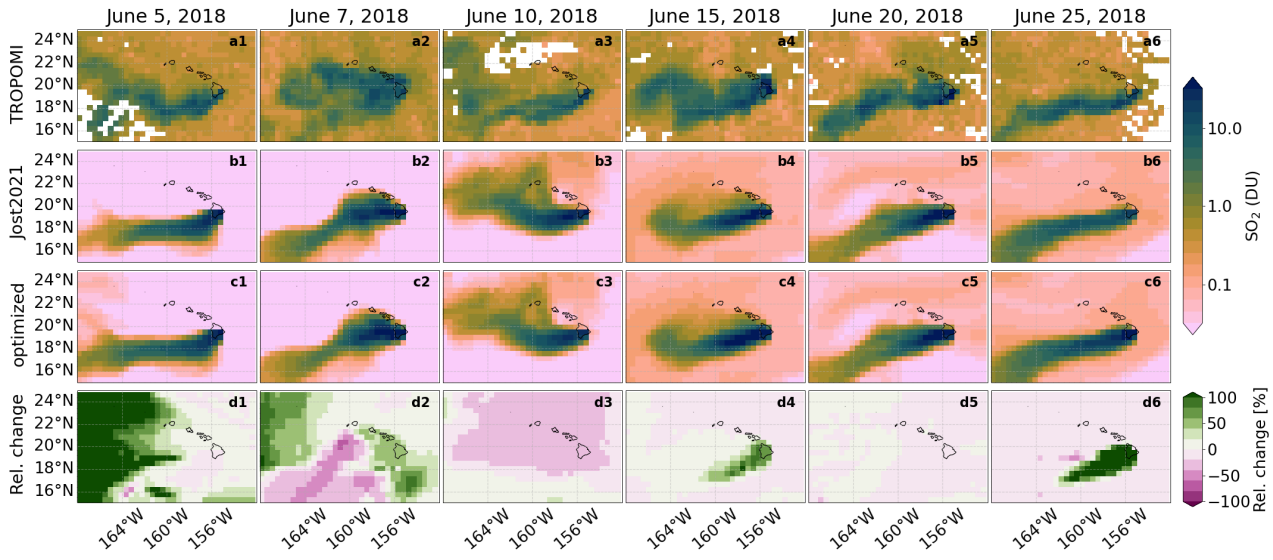

Figure 9. Observed (top) and simulated SO_2 columns resulting from the degassing of the Kilauea volcano at selected days in June 2018 at a model resolution of T255. **a*,** Observations from TROPOMI, regridded to T255 resolution. **b*,** Simulation with emission rates derived by Jost (2021, scaled by a factor of 4.3 – see text for details). **c*,** Simulation with optimized emission rates, based on a comparison between model and observations (refer to the text for more details). **d*,** Relative change from the simulation with derived emission rates by Jost (2021) to the optimized simulation.

at each day in June 2018 d (bottom), and spatial correlation between simulated and observed logarithmic SO_2 columns (top) within this horizontal window. The **Jost2021** numerical results exhibits some noticeable fluctuations in $\overline{SO_{2(\mathtt{col},d)}}$, with periods of underestimation in the initial days and on June 25, as well as instances of significant overestimation, such as on June 11 and June 21. The presence of a low-bias can be primarily attributed to missing or very low emission data from Jost (2021) due to missing orbits or cloud cover hindering reasonable SO_2 retrieval. As expected, the simulated $\overline{SO_{2(\mathtt{col},d)}}$ from the **optimized** simulation follows the observed pattern much more closely as a result of the tuning.

On most days, a strong spatial correlation between the simulated and observed horizontal dispersion of the SO_2 plume is evident, ranging from 0.6 to 0.9. However, the pronounced exceptions on June 7 and June 10 (also depicted in Fig. 9) may be attributed to misrepresentations of the meteorological conditions or generally lower wind speeds, leading to more turbulent flow. Barely any improvement in spatial correlation can be observed from the **Jost2021** simulation to the **optimized** one. This lack of difference is primarily due to the intra-day fluctuations of SO_2 emissions, which contribute to the observed variations and are also not accounted for in the optimized simulation, and potential differences in injection height, that are not considered in the simulation. To address the former, emission rates would need to be implemented at higher temporal resolution (e. g. hourly) and the simulations would need to be performed at higher horizontal resolution.

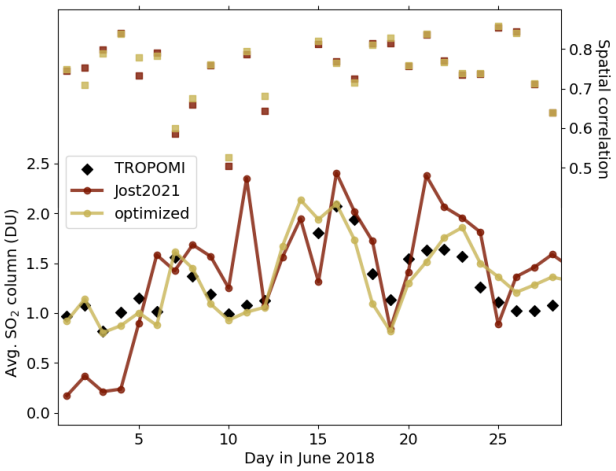

Figure 10. Derived spatially averaged SO_2 column from TROPOMI observations ($-168°$ to $-152°$ W, $15°$ to $25°$ N; horizontal window displayed in Fig. 9) in June 2018 compared with simulations, using emission rates from Jost (2021, scaled by a factor of 4.3 – see text for details) and optimized emission rates, based on a comparison between model and observations. On the top, we present spatial correlations in the same horizontal window between the observations and the respective simulations, using the same color as for the SO_2 column.

5 Discussion

We showed that SO_2 emissions from explosive volcanic eruptions and the subsequent plume evolution can be reasonably reproduced in EMAC within the MESSy model system, using either 3D emissions (Schallock et al., 2023) derived from satellite observations, or column emissions with differing vertical profiles. The different approaches exhibit strengths and weaknesses, and reveal information on the general capabilities of the model.

The usage of 3D emissions, as investigated by Schallock et al. (2023), offers significant advantages for assessing the mid- and long-term impact of volcanic eruptions. By directly deriving emissions from 3D satellite observations several days after the initial eruption, this approach ensures an accurate representation of the plume's horizontal and vertical evolution, particularly during the crucial initial phase post-eruption, which is heavily influenced by local meteorological conditions. However, a notable drawback of this method is the inherent limitation in the vertical sensitivity of the satellite observations, leading to an overestimation of the vertical extent of the plume, and thus not reproducing the real distribution. Consequently, this discrepancy impacts the plume's subsequent evolution and results in differing stratospheric lifetimes for the volcanic plume. Additionally, due to the reliance on 3D satellite observations and the delayed injection, short-term volcanic effects cannot be adequately examined for the simulation with 3D emissions. Another limitation of the approach outlined by Schallock et al. (2023) lies in its technical implementation, which necessitates manual addition of retrieved tracer perturbations and subsequent model restarts after each volcanic event or the use of large import files, posing practical challenges for operational use.

Column emissions rely on several assumptions regarding critical parameters such as plume height and location, emitted mass, and emission profile. With sufficient observational data, these parameters can be effectively constrained, enabling accurate

predictions of SO_2 mixing ratios. However, the creation and updating of such inventories also needs manual work, retrieving the relevant parameters. As demonstrated with the Nabro volcano, we used data from the volcanic SO_2 emission inventory compiled by Schallock et al. (2023) in combination with observations from IASI to accurately constrain these parameters. Consequently, our model simulations exhibited strong agreement with both, short- and mid-term observations of SO_2 mixing ratios and aerosol optical properties obtained from the IASI, MIPAS, and OSIRIS satellite instruments, specifically evaluated for strong eruptions.

The sensitivity studies revealed that the importance of accurately constraining the emission parameters for adequately simulating the volcanic SO_2 plume differs for each parameter. Primarily, emitting an appropriate quantity of SO_2 at the correct altitude appears to be the most critical factor. Variations in the SO_2 amount directly influence stratospheric SO_2 mixing ratios, with the mixing ratios approximately proportional to the mass emitted. Conversely, discrepancies in the injection altitude substantially impact the stratospheric lifetime of the resulting SO_2 and sulfur aerosol, as well as the meteorological conditions encountered by the plume.

For that reason, we opted for the emission database developed by Brühl et al. (2018) and Schallock et al. (2023) for the historic default namelist setup, as they specifically target SO_2 injections above the tropopause, while the databases from Diehl et al. (2012) and Carn et al. (2017) do not distinguish between the tropospheric and stratospheric part of the plume, providing no information about the SO_2 amount above the tropopause. Mills et al. (2016) do provide a minimum and maximum plume altitude, however potentially underestimate the stratospheric part when uniformly emitting over this altitude range as can be seen in the sensitivity study on the Nabro volcano (see Sect. 4.1.2). The unclear stratospheric contribution of the initial SO_2 emission is also the main reason for the vastly differing stratospheric sulfur burden estimated by Brodowsky et al. (2021) from the different emission databases, again highlighting the importance of the correct retrieval and application of the stratospheric part of the plume. The emission database from Schallock et al. (2023) additionally explicitly includes smaller eruptions reaching the stratosphere.

However, column or point emissions come with inherent limitations as well. First, emissions are constrained to a single grid box or columns of grid boxes in this study, potentially resulting in localized and exaggerated mixing ratios of SO_2, when volcanic plumes span areas exceeding one grid box (Tilmes et al., 2023). This may lead to a depletion of the oxidants, and subsequently to a slower oxidation to H_2SO_4. While distributing emissions on multiple columns horizontally may mitigate this effect by defining multiple emission points per eruption (Tilmes et al., 2023), we did not explore this aspect in our analysis. However, in detailed studies of strong eruptions, we additionally recommend exploring the effects of emissions over multiple columns and an extended time period to avoid non-linearities due to very high concentrations (see also Sect. 2.1.2).

Second, volcanic activity typically extends beyond a single day, with SO_2 emissions occurring over prolonged periods, occasionally reaching the stratosphere. The identification and appropriate mass allocation across multiple entry points pose challenges for automation. In the case of the Nabro eruption, our observations from IASI revealed two distinct stratospheric entry points. We observed discrepancies in the short-term evolution of SO_2 between the reference simulation, which considered only one stratospheric entry point, and the optimized simulation, which distributed emissions across two entry points. While

these differences dissipated in the mid-term, it is important to note that this outcome may not be necessarily applicable to all volcanic eruptions.

Third, it is important to note that detailed data regarding the precise timing and geographical coordinates of the stratospheric entry, as derived from IASI, is not accessible for all volcanic eruptions. Smaller eruptions, in particular, often fall below the detection threshold of IASI, and IASI only became operational in 2007. Our sensitivity analyses, varying the timing and geographical positioning of the plume entry into the stratosphere, uncovered short- and mid-term disparities when such information is lacking.

Based on the insights from the sensitivity studies, we developed a historical namelist configuration for the new EVER submodel spanning the past three decades. Despite the aforementioned limitations, our evaluation simulation demonstrates a satisfactory alignment with observations of both, SO_2 mixing ratios and aerosol optical properties. Notably, the historic namelist setup accurately reproduces significant eruptions, thereby representing the primary contribution of volcanic events to the stratospheric SO_2 and aerosol loading. This aligns with our conclusion that altitude and mass are the most crucial emission parameters, which were directly determined from the emission inventory and do not depend on the availability of IASI observations. However, we showed that the timing and geographical location of the stratospheric entry point can lead to additional uncertainties, that remain when no IASI observations are available.

Consequently, we recommend the adoption of the submodel EVER with the proposed historical namelist setup (see Sect. 2.2 and supplement) in all numerical simulations using the MESSy framework at global or regional scale, particularly those encompassing the stratospheric and upper tropospheric domains. This is the first study to systematically incorporate volcanic eruptions into atmospheric simulations within MESSy using the EMAC model, presenting a more flexible and easy-to-implement alternative to the 3D emission approach. Furthermore, in cases where disparities with observations arise, owing to the aforementioned uncertainties, or when focusing on specific volcanic events, the namelist setup can be adjusted accordingly, especially regarding the horizontal and vertical extent of the plume. Moreover, comparisons with simulations using 3D emission fields may offer additional insights into the evolution of individual volcanic plumes.

In section 4.3, we demonstrated the additional capability of EVER to simulate SO_2 from degassing volcanoes. However, it is essential to apply a model with a sufficiently fine resolved horizontal grid (for a global model) to accurately capture the observed phenomena and the small-scale wind fluctuations. Simulations with equal emissions performed at more standard horizontal resolutions, such as T63 and T106, failed to reproduce the observations adequately (not shown), whereas these resolutions are mostly sufficient for stratospheric simulations. Furthermore, we applied a model-driven tuning for the corresponding emission rates, reproducing observed SO_2 column amounts.

This optimization has the potential to be extended to historic degassing volcanoes, facilitating the development of a default setup akin to the stratospheric default setup for explosive volcanoes. This process would include integrating TROPOMI observations with an initial simulation using rough estimates of degassing emissions, which could subsequently be refined through stochastic gradient descent (SGD) optimization as described in Appendix B, potentially extending or replacing the outdated climatology by Diehl et al. (2012) used in many EMAC simulations. However, implementing this approach may encounter

challenges related to the required high horizontal resolution, the estimation of the injection altitude, and the identification and initial approximate estimation of all significant degassing volcano emissions.

Up to this point, our focus has been primarily on volcanic SO_2. However, it is worth mentioning the versatility of the submodel for a wide range of use cases where gaseous or aerosol tracers are injected into the atmosphere in vertical distributions, with limited horizontal extent. This includes the following use cases:

- **Volcanic ash:** Apart from emitting trace gases, volcanic eruptions also release primary aerosols, such as volcanic ash. The EVER submodel is explicitly designed to simulate the evolution of aerosol species, including volcanic ash, after volcanic eruptions.
- **Water vapor:** Eruptions of submarine volcanoes, such as the notable event at Hunga Tonga-Hunga Ha'apai in January 2022 (e.g., Vömel et al., 2022; Sellitto et al., 2022; Schoeberl et al., 2022; Xu et al., 2022), release substantial quantities of water vapor into the atmosphere. The EVER module can be used to investigate the effects of enhanced water vapor concentrations in the stratosphere due to volcanic activity. For the Hunga Tonga eruption we recommend the simultaneous injection of water vapor in multiple columns to avoid quick removal by ice formation and to be consistent with observations.
- **Wildfires:** Strong wildfires can inject significant amounts of carbonaceous aerosols and various trace gases directly into the stratosphere via pyro-cumulonimbi. EVER can be used to model these emissions from wildfires.
- **Solar radiation modification:** Studies on solar radiation modification, particularly artificial injections of SO_2 or other trace gases into the stratosphere to form aerosols that reflect sunlight back into space, can benefit from the capabilities of EVER. These scenarios involve large uncertainties, which can be addressed with studies using EVER.
- **Transport processes:** Transport processes play a crucial role throughout the atmosphere. EVER allows for the emission of active and passive aerosols and trace gases throughout the atmosphere, enabling the study of processes such as the exchange between the troposphere and stratosphere.
- **Sensitivity studies:** Atmospheric properties can be highly sensitive to perturbations in trace gas or aerosol mixing ratios. By injecting the respective atmospheric constituents with EVER, it is possible to estimate the sensitivity of climate, atmospheric dynamics, and the ozone column to these perturbations.

6 Conclusions

We presented the new submodel for tracer emissions from Explosive Volcanic ERuptions (EVER v1.1), developed within the Modular Earth Submodel System (MESSy, version 2.55.1), and performed numerical experiments with the ECHAM5/MESSy Atmospheric Model (EMAC) and the new submodel.

EVER is designed for the addition of gaseous and aerosol tracer tendencies following volcanic eruptions in columns with user-specified vertical profiles at point or area sources. We evaluated the EVER submodel with the simulation of volcanic

SO_2 emissions in the EMAC model for the explosive eruption of Nabro in June 2011 and a degassing event from Kilauea in July 2018, employing satellite observations from IASI, MIPAS, OMI, TROPOMI, and OSIRIS. The evaluation showed that volcanic emission plumes can be reasonably simulated with EVER. The new submodel is available from MESSy version 2.55.1 and will be continuously developed further.

We investigated the sensitivity of the volcanic SO_2 plume evolution after the Nabro eruption to variations in the emission parameters. The results emphasized the importance of the emission of a reasonable amount of SO_2 above the tropopause with an appropriate altitude distribution. In previous studies with various emission databases, the SO_2 mass emitted in the stratosphere was unclear, resulting in large differences. We showed that the application of a dedicated stratospheric SO_2 emission inventory can reproduce observed SO_2 burdens and aerosol optical properties. Horizontal position and emission timing were found to have a minor impact on the mid-term SO_2 burden in the stratosphere. Nevertheless, these parameters play a crucial role in detailed process studies during the initial weeks after an eruption.

Furthermore, we conclude that simulations of volcanic eruptions can be effectively performed with the help of 3D- and column emissions, if the emitted stratospheric SO_2 mass is well constrained. However, both approaches have shortcomings. The optimal approach depends on the specific use case, with column emissions excelling in the short-term, and similar performance in the mid- to long-term.

Finally, we developed a historic submodel setup for EVER, incorporating stratospheric significant volcanic eruptions spanning from 1990 to 2023. It is based on the volcanic SO_2 emission inventory by Schallock et al. (2023). We additionally optimized the timing and geographical location of the volcanic plume entering the stratosphere, using the findings of the sensitivity study and SO_2 observations from the IASI satellite. However, this information was only available from 2007 on, and for strong volcanic eruptions only. The historic namelist setup was successfully evaluated with regard to resulting SO_2 mixing ratios and aerosol optical properties. It is provided as a supplement, and we advocate its inclusion in simulations using the MESSy framework focusing on the upper troposphere and the stratosphere. For very strong eruptions, it may be beneficial to distribute the emissions over multiple columns horizontally and an extended time period, or adjust the vertical plume extent, if discrepancies with observations occur.

In addition to the extensively discussed application to explosive volcanic eruptions, the EVER submodel's versatility opens up a range of additional research opportunities. These may include investigations into the interplay between SO_2 and volcanic ash post-eruption, exploration of solar radiation modification scenarios, modelling of wildfires, and analyses of atmospheric transport processes. Future work could involve the development of a climatology of SO_2 emissions from degassing volcanoes employing the new submodel.

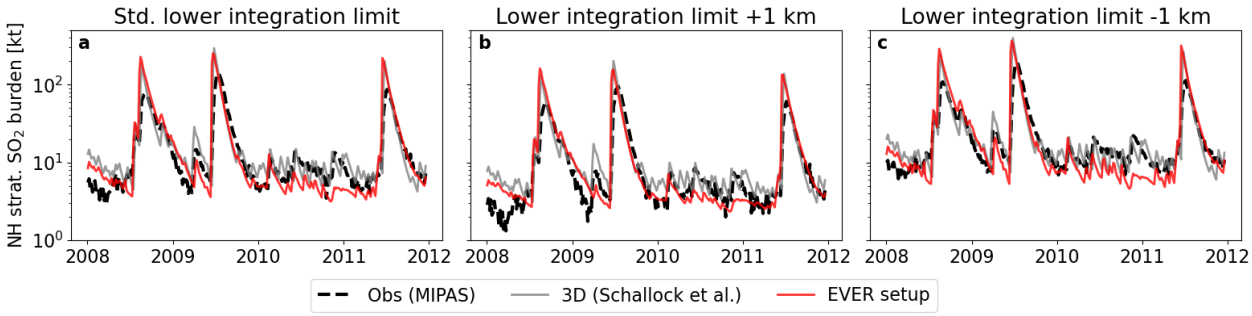

Figure A1. Sensitivity of the evaluation results to the lower integration limit (applied to observations and simulations) for the derivation of the stratospheric SO_2 burden. **a,** Lower integration limit as applied in the manuscript (16 km from 0-30°N, 14 km from 30-60°N and 12 km from 60-90°N). Variations of plus 1 km (**b**) and minus 1 km (**c**) show similar agreement at different absolute values. Slight differences can be seen at background levels with increased agreement in 2010 for the increased lower integration limit (**b**).

Appendix A: Sensitivity of the evaluation results to the lower integration limit for the calculation of stratospheric properties

As the tropopause does not necessarily coincide in the simulation and the observations, we applied latitude-dependent fixed altitude lower integration limits for the calculation of stratospheric SO_2 burden and sAOD. Here, we study the sensitivity of the evaluation results to the chosen lower integration limit.

The stratospheric SO_2 burden is defined in this work as the SO_2 mass above 16 km from 0-30°, above 14 km from 30-60°, and above 12 km from 60-90°. We compare these stratospheric SO_2 burdens to burdens with perturbed lower integration limits (+1 km: 17,15,13 km; -1 km: 15,13,11 km). The results are depicted in Fig. A1. While the total burden varies in the three scenarios as expected, the agreement between the simulations and the observations is very similar, especially considering the three major volcanic peaks. However, in the quiet period in 2010 and 2011, the agreement improves, when the lower integration limit increases (b). This can be either attributed to an incorrect altitude distribution of the background SO_2 or to the emission of the smaller eruptions.

The sAOD is defined here as the integral over the aerosol extinction above 16 km from 0-25°, and above 12 km from 45-80°. As before, we vary this lower integration limit by ± 1 km (see Fig. A2). Again, we see similar agreement at differing absolute values. The strongest difference can be seen in the Sarychev peak at higher latitudes (e), that seems to be underestimated when increasing the lower integration limit. This might either be connected to the missing AKM, or the plume top is underestimated.

Overall, we conclude, that our evaluation result are not very sensitive to the cosen lower integration limit for the calculation of the stratospheric SO_2 burden and the sAOD. Thus, the evalaution results are mostly independent on the chosen "tropopause definition".

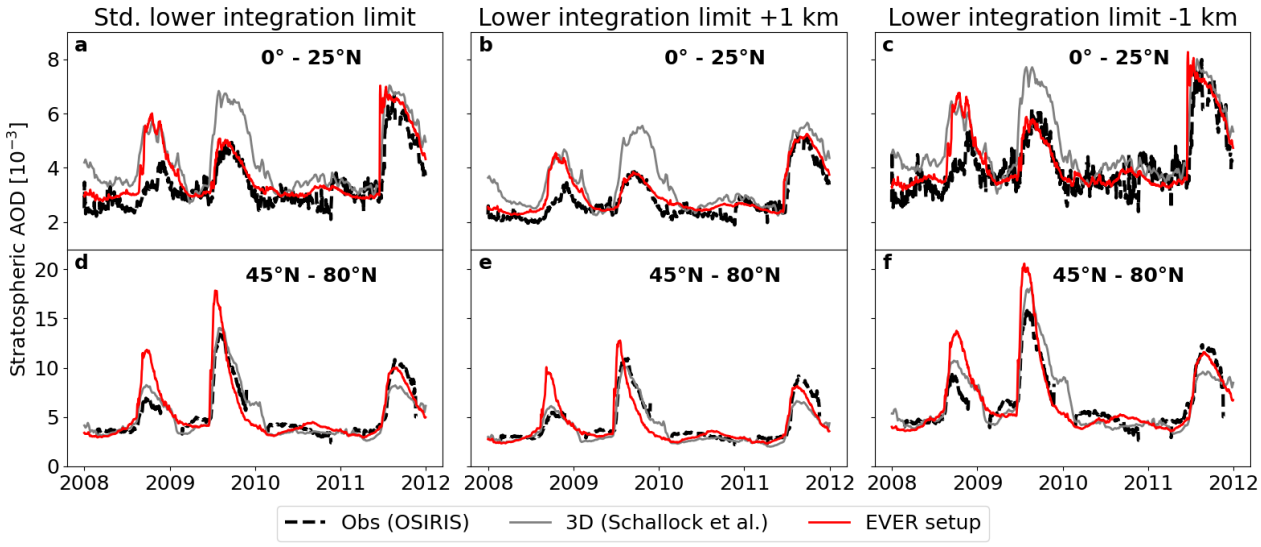

Figure A2. Sensitivity of the evaluation result to the lower integration limit (applied to observations and simulations) for the derivation of sAOD. **a,d** Lower integration limit as applied in the manuscript (16 km from 0-25°N and 12 km from 45-80°N). Variations of plus 1 km (**b,e**) and minus 1 km (**c,f**) show similar agreement at different absolute values. The most significant differences are observed for the Sarychev volcano, that shows strongly decreased simulated sAOD at increased lower integration limit at higher latitudes (**e**).

Appendix B: Optimization of the emission rates from the Kilauea degassing event

In Sect. 4.3, we optimized the emission rates of the Kilauea volcano, such that the model reproduces the observed average SO_2 column $\overline{SO_{2(\mathrm{col},d,\mathrm{obs})}}$ for each day d over the chosen area. Here, the optimization is described in more detail.

In the first step, we investigated the relation between the implemented emission rates and resulting simulated $\overline{SO_{2(\mathrm{col},d,\mathrm{sim})}}$. Therefore, we considered the emission rates from the three preceding days of each sampled day in June 2018, denoted as $\mathrm{emis}_{SO_2;d-i} (i = 0, 1, 2)$, and constructed a linear predictor of $\overline{SO_{2(\mathrm{col},d)}}$:

$$\overline{SO_{2(\mathrm{col},d,\mathrm{sim})}} = SO_{2(\mathrm{col,BG})} + \sum_{i=0}^{3} a_{d-i} * \mathrm{emis}_{SO_2;d-i} \tag{B1}$$

The coefficients a_{d-i}, representing the importance of the emissions of each of the three preceding days, respectively, and the background SO_2 column amount, $SO_{2(\mathrm{col,BG})}$, are the free parameters in the linear predictor and were determined through a least squares fit. Subsequently, the linear predictor with these coefficients was utilized to compute optimized emission rates for each day using a stochastic gradient descent (SGD) algorithm, iteratively optimizing the emission rates, by reducing the loss function (e. g. Ruder, 2016). The optimization scheme is given in pseudocode in Algorithm B1.

Algorithm B1 SGD optimizer for daily SO_2 emission rates

Require: `niter,lrate`

while `j<niter` **do**
  for `d=0,d<30,k++` **do**
    for `k=0,k<3,k++` **do**
      $\texttt{gradient}=2*\texttt{a}_{\texttt{d-k}}*(\texttt{SO}_{2(\texttt{col},d\texttt{obs})} - \sum_{\texttt{i=0}}^{2} \texttt{a}_{\texttt{d-i}}*\texttt{emis}_{\texttt{SO}_2\texttt{;d-i}} - \texttt{SO}_{2(\texttt{col,BG})})$
      $\texttt{emis}_{\texttt{SO}_2\texttt{;d-k}}\texttt{+=lrate}*\texttt{gradient}$
    end for
  end for
  `j++`
end while

Code availability. The Modular Earth Submodel System (MESSy, https://zenodo.org/doi/10.5281/zenodo.8360186) is continuously further developed and applied by a consortium of institutions. The usage of MESSy and access to the source code is licenced to all affiliates of institutions which are members of the MESSy Consortium. Institutions can become a member of the MESSy Consortium by signing the MESSy Memorandum of Understanding. More information can be found on the MESSy Consortium Website (http://www.messy-interface.org). The code presented here is available in MESSy version 2.55.1 (https://zenodo.org/records/8367075). The respective namelists, chemical mechanisms and run scripts used are made available via supplement (see Sect. 3.2).

Scientific colour maps (https://doi.org/10.5281/zenodo.5501399, Crameri, 2021) are used in this study to prevent visual distortion of the data and exclusion of readers with colour vision deficiencies (Crameri et al., 2020).

The historic default namelist setup for the new submodel EVER is available as supplement (*ever_historic_stratVolcanoes.nml*).

Data availability. Level 2 and Level 3 (5-day averages) retrieved (V5R_SO2_220 & V5R_SO2_221) SO_2 data from MIPAS observations used in this study is available after registration at http://www.imk-asf.kit.edu/english/308.php (Höpfner et al., 2013, 2015). Level 2 OMI SO_2 observations (v003) are taken from https://disc.gsfc.nasa.gov/datasets/OMSO2_003/summary (Li et al., 2020). IASI SO_2 products (linear product version 2) are available at https://doi.org/10.25326/41 (Clarisse, 2023). We obtained the OSIRIS aerosol product version 7.2 from https://research-groupstest.usask.ca/osiris/data-products.php (Rieger et al., 2019). The TROPOMI Level 2 SO_2 product (repro, v1.1) is publicly available at https://doi.org/10.5270/S5P-yr8kdpp (ESA, 2018). Model output and setups are archived at the DKRZ in Hamburg, and are available on request. The historic SO_2 emission inventory of explosive volcanic eruptions is available at https://doi.org/10.26050/WDCC/SSIRC_3 (Brühl et al., 2021; Schallock et al., 2023).

Author contributions. MK and AP planned the research. MK developed the EVER submodel with the help of AP and PJ. JS and CB provided the emission inventory, performed the simulation with 3D emissions, and assisted in the provision of satellite data and information on volcanoes. AJ and SB provided the daily SO_2 emission rates for the Kilauea volcano. MH provided the MIPAS observations with the respective averaging kernel matrix. MK evaluated the simulations, analysed the model results, developed the historic namelist setup, and wrote the manuscript. AP and HT supervised the project. All authors discussed the results and contributed to the review and editing of the manuscript.

Competing interests. Two co-authors are member of the editorial board of Geoscientific Model Developments.

Acknowledgements. MK acknowledges the financial support of the Max Planck Graduate Center with the Johannes Gutenberg University (Mainz). The model simulations have been performed at the German Climate Computing Centre (DKRZ) through support from the Max Planck Society. We acknowledge the effort of Michael Kiefer to supply the Averaging Kernel Matrices for the SO_2 product from MIPAS. HT acknowledges funding support from the Deutsche Forschungsgemeinschaft (DFG, German Research Foundation) – TRR 301 – Project-ID 428312742.

References

Beirle, S., Hörmann, C., Penning de Vries, M., Dörner, S., Kern, C., and Wagner, T.: Estimating the volcanic emission rate and atmospheric lifetime of SO_2 from space: a case study for Kīlauea volcano, Hawai'i, Atmospheric Chemistry and Physics, 14, 8309–8322, https://doi.org/10.5194/acp-14-8309-2014, 2014.

Beirle, S., Borger, C., Dörner, S., Li, A., Hu, Z., Liu, F., Wang, Y., and Wagner, T.: Pinpointing nitrogen oxide emissions from space, Science Advances, 5, https://doi.org/10.1126/sciadv.aax9800, 2019.

Beirle, S., Borger, C., Jost, A., and Wagner, T.: Improved catalog of NO_x point source emissions (version 2), Earth System Science Data, 15, 3051–3073, https://doi.org/10.5194/essd-15-3051-2023, 2023.

Bourassa, A. E., Robock, A., Randel, W. J., Deshler, T., Rieger, L. A., Lloyd, N. D., Llewellyn, E. J. T., and Degenstein, D. A.: Large Volcanic Aerosol Load in the Stratosphere Linked to Asian Monsoon Transport, Science, 337, 78–81, https://doi.org/10.1126/science.1219371, 2012.

Bourassa, A. E., Robock, A., Randel, W. J., Deshler, T., Rieger, L. A., Lloyd, N. D., Llewellyn, E. J., and Degenstein, D. A.: Response to Comments on "Large Volcanic Aerosol Load in the Stratosphere Linked to Asian Monsoon Transport", Science, 339, 647–647, https://doi.org/10.1126/science.1227961, 2013.

Brodowsky, C., Sukhodolov, T., Feinberg, A., Höpfner, M., Peter, T., Stenke, A., and Rozanov, E.: Modeling the Sulfate Aerosol Evolution After Recent Moderate Volcanic Activity, 2008–2012, Journal of Geophysical Research: Atmospheres, 126, e2021JD035 472, https://doi.org/https://doi.org/10.1029/2021JD035472, 2021.

Brühl, C., Schallock, J., Klingmüller, K., Robert, C., Bingen, C., Clarisse, L., Heckel, A., North, P., and Rieger, L.: Stratospheric aerosol radiative forcing simulated by the chemistry climate model EMAC using Aerosol CCI satellite data, Atmospheric Chemistry and Physics, 18, 12 845–12 857, https://doi.org/10.5194/acp-18-12845-2018, 2018.

Brühl, C., Schallock, J., and Diehl, T.: Volcanic SO2 data derived from limb viewing satellites for the lower stratosphere from 1990 to 2019, and from nadir viewing satellites for the troposphere, including the corresponding radiative forcing computed by the CCM EMAC, World Data Center for Climate (WDCC) at DKRZ [data set], https://doi.org/10.26050/WDCC/SSIRC_3, 2021.

Carn, S., Clarisse, L., and Prata, A.: Multi-decadal satellite measurements of global volcanic degassing, Journal of Volcanology and Geothermal Research, 311, 99–134, https://doi.org/10.1016/j.jvolgeores.2016.01.002, 2016.

Carn, S., Fioletov, V., McLinden, C., Li, C., and Krotkov, N.: A decade of global volcanic SO2 emissions measured from space, Scientific reports, 7, 44 095, https://doi.org/10.1038/srep44095, 2017.

Clarisse, L.: Daily IASI/Metop-A ULB-LATMOS sulphur dioxide (SO2) L2 product (columns and altitude, Aeris) [data set], https://doi.org/10.25326/41, 2023.

Clarisse, L., Hurtmans, D., Clerbaux, C., Hadji-Lazaro, J., Ngadi, Y., and Coheur, P.-F.: Retrieval of sulphur dioxide from the infrared atmospheric sounding interferometer (IASI), Atmospheric Measurement Techniques, 5, 581–594, https://doi.org/10.5194/amt-5-581-2012, 2012.

Clarisse, L., Coheur, P.-F., Theys, N., Hurtmans, D., and Clerbaux, C.: The 2011 Nabro eruption, a SO_2 plume height analysis using IASI measurements, Atmospheric Chemistry and Physics, 14, 3095–3111, https://doi.org/10.5194/acp-14-3095-2014, 2014.

Crameri, F.: Scientific colour maps, Zenodo [code], https://doi.org/10.5281/zenodo.5501399, 2021.

Crameri, F., Shephard, G. E., and Heron, P. J.: The misuse of colour in science communication, Nature communications, 11, 1–10, https://doi.org/10.1038/s41467-020-19160-7, 2020.

Diehl, T., Heil, A., Chin, M., Pan, X., Streets, D., Schultz, M., and Kinne, S.: Anthropogenic, biomass burning, and volcanic emissions of black carbon, organic carbon, and SO_2 from 1980 to 2010 for hindcast model experiments, Atmospheric Chemistry and Physics Discussions, 12, 24 895–24 954, https://doi.org/10.5194/acpd-12-24895-2012, 2012.

Dietmüller, S., Jöckel, P., Tost, H., Kunze, M., Gellhorn, C., Brinkop, S., Frömming, C., Ponater, M., Steil, B., Lauer, A., and Hendricks, J.: A new radiation infrastructure for the Modular Earth Submodel System (MESSy, based on version 2.51), Geoscientific Model Development, 9, 2209–2222, https://doi.org/10.5194/gmd-9-2209-2016, 2016.

Durand, M. and Grattan, J.: Effects of volcanic air pollution on health, The Lancet, 357, 164, https://doi.org/10.1016/S0140-6736(00)03586-8, 2001.

European Space Agency (ESA): Copernicus Sentinel-5P (processed by ESA), TROPOMI Level 2 Sulphur Dioxide Total Column. Version 01., https://doi.org/10.5270/S5P-yr8kdpp, 2018.

Fountoukis, C. and Nenes, A.: ISORROPIA II: a computationally efficient thermodynamic equilibrium model for K^+–Ca^{2+}–Mg^{2+}–$NH_4{}^+$–Na^+–$SO_4{}^-$–$NO_3{}^-$–Cl^-–H_2O aerosols, Atmospheric Chemistry and Physics, 7, 4639–4659, https://doi.org/10.5194/acp-7-4639-2007, 2007.

Fromm, M., Nedoluha, G., and Charvát, Z.: Comment on "Large Volcanic Aerosol Load in the Stratosphere Linked to Asian Monsoon Transport", Science, 339, 647–647, https://doi.org/10.1126/science.1228605, 2013.

Giorgetta, M. A., Manzini, E., and Roeckner, E.: Forcing of the quasi-biennial oscillation from a broad spectrum of atmospheric waves, Geophysical Research Letters, 29, 86–1–86–4, https://doi.org/https://doi.org/10.1029/2002GL014756, 2002.

Global Volcanism Program: Report on Nabro (Eritrea) (Wunderman, R., ed.), Bulletin of the Global Volcanism Network, 36:9, https://doi.org/10.5479/si.GVP.BGVN201109-221101, 2011.

Hersbach, H., Bell, B., Berrisford, P., Hirahara, S., Horányi, A., Muñoz-Sabater, J., Nicolas, J., Peubey, C., Radu, R., Schepers, D., Simmons, A., Soci, C., Abdalla, S., Abellan, X., Balsamo, G., Bechtold, P., Biavati, G., Bidlot, J., Bonavita, M., De Chiara, G., Dahlgren, P., Dee, D., Diamantakis, M., Dragani, R., Flemming, J., Forbes, R., Fuentes, M., Geer, A., Haimberger, L., Healy, S., Hogan, R. J., Hólm, E., Janisková, M., Keeley, S., Laloyaux, P., Lopez, P., Lupu, C., Radnoti, G., de Rosnay, P., Rozum, I., Vamborg, F., Villaume, S., and Thépaut, J.-N.: The ERA5 global reanalysis, Quarterly Journal of the Royal Meteorological Society, 146, 1999–2049, https://doi.org/https://doi.org/10.1002/qj.3803, 2020.

Hommel, R., Timmreck, C., Giorgetta, M. A., and Graf, H. F.: Quasi-biennial oscillation of the tropical stratospheric aerosol layer, Atmospheric Chemistry and Physics, 15, 5557–5584, https://doi.org/10.5194/acp-15-5557-2015, 2015.

Höpfner, M., Glatthor, N., Grabowski, U., Kellmann, S., Kiefer, M., Linden, A., Orphal, J., Stiller, G., von Clarmann, T., Funke, B., and Boone, C. D.: Sulfur dioxide (SO_2) as observed by MIPAS/Envisat: temporal development and spatial distribution at 15–45 km altitude, Atmospheric Chemistry and Physics, 13, 10 405–10 423, https://doi.org/10.5194/acp-13-10405-2013, 2013.

Höpfner, M., Boone, C. D., Funke, B., Glatthor, N., Grabowski, U., Günther, A., Kellmann, S., Kiefer, M., Linden, A., Lossow, S., Pumphrey, H. C., Read, W. G., Roiger, A., Stiller, G., Schlager, H., von Clarmann, T., and Wissmüller, K.: Sulfur dioxide (SO_2) from MIPAS in the upper troposphere and lower stratosphere 2002–2012, Atmospheric Chemistry and Physics, 15, 7017–7037, https://doi.org/10.5194/acp-15-7017-2015, 2015.

Intergovernmental Panel on Climate Change (IPCC): Climate Change 2021 – The Physical Science Basis: Working Group I Contribution to the Sixth Assessment Report of the Intergovernmental Panel on Climate Change, Cambridge University Press, https://doi.org/10.1017/9781009157896, 2023.

Jeuken, A. B. M., Siegmund, P. C., Heijboer, L. C., Feichter, J., and Bengtsson, L.: On the potential of assimilating meteorological analyses in a global climate model for the purpose of model validation, Journal of Geophysical Research: Atmospheres, 101, 16 939–16 950, https://doi.org/10.1029/96JD01218, 1996.

Jöckel, P., Tost, H., Pozzer, A., Brühl, C., Buchholz, J., Ganzeveld, L., Hoor, P., Kerkweg, A., Lawrence, M. G., Sander, R., Steil, B., Stiller, G., Tanarhte, M., Taraborrelli, D., van Aardenne, J., and Lelieveld, J.: The atmospheric chemistry general circulation model ECHAM5/MESSy1: consistent simulation of ozone from the surface to the mesosphere, Atmospheric Chemistry and Physics, 6, 5067–5104, https://doi.org/10.5194/acp-6-5067-2006, 2006.

Jöckel, P., Kerkweg, A., Buchholz-Dietsch, J., Tost, H., Sander, R., and Pozzer, A.: Technical Note: Coupling of chemical processes with the Modular Earth Submodel System (MESSy) submodel TRACER, Atmospheric Chemistry and Physics, 8, 1677–1687, https://doi.org/10.5194/acp-8-1677-2008, 2008.

Jöckel, P., Kerkweg, A., Pozzer, A., Sander, R., Tost, H., Riede, H., Baumgaertner, A., Gromov, S., and Kern, B.: Development cycle 2 of the Modular Earth Submodel System (MESSy2), Geoscientific Model Development, 3, 717–752, https://doi.org/10.5194/gmd-3-717-2010, 2010.

Jost, A.: Determining the SO_2 emission rates of the Kilauea volcano in Hawaii using S5P-TROPOMI satellite measurements, Bachelor's thesis, Johannes Gutenberg Universität Mainz, 2021.

Kaiser, J. C., Hendricks, J., Righi, M., Riemer, N., Zaveri, R. A., Metzger, S., and Aquila, V.: The MESSy aerosol submodel MADE3 (v2.0b): description and a box model test, Geoscientific Model Development, 7, 1137–1157, https://doi.org/10.5194/gmd-7-1137-2014, 2014.

Kaiser, J. C., Hendricks, J., Righi, M., Jöckel, P., Tost, H., Kandler, K., Weinzierl, B., Sauer, D., Heimerl, K., Schwarz, J. P., Perring, A. E., and Popp, T.: Global aerosol modeling with MADE3 (v3.0) in EMAC (based on v2.53): model description and evaluation, Geoscientific Model Development, 12, 541–579, https://doi.org/10.5194/gmd-12-541-2019, 2019.

Kerkweg, A., Sander, R., Tost, H., and Jöckel, P.: Technical note: Implementation of prescribed (OFFLEM), calculated (ONLEM), and pseudo-emissions (TNUDGE) of chemical species in the Modular Earth Submodel System (MESSy), Atmospheric Chemistry and Physics, 6, 3603–3609, https://doi.org/10.5194/acp-6-3603-2006, 2006.

Kern, C., Lerner, A. H., Elias, T., Nadeau, P. A., Holland, L., Kelly, P. J., Werner, C. A., Clor, L. E., and Cappos, M.: Quantifying gas emissions associated with the 2018 rift eruption of Kīlauea Volcano using ground-based DOAS measurements, Bulletin of Volcanology, 82, 55, https://doi.org/10.1007/s00445-020-01390-8, 2020.

Klobas, J. E., Wilmouth, D. M., Weisenstein, D. K., Anderson, J. G., and Salawitch, R. J.: Ozone depletion following future volcanic eruptions, Geophysical Research Letters, 44, 7490–7499, https://doi.org/10.1002/2017GL073972, 2017.

Kohl, M., Lelieveld, J., Chowdhury, S., Ehrhart, S., Sharma, D., Cheng, Y., Tripathi, S. N., Sebastian, M., Pandithurai, G., Wang, H., and Pozzer, A.: Numerical simulation and evaluation of global ultrafine particle concentrations at the Earth's surface, Atmospheric Chemistry and Physics, 23, 13 191–13 215, https://doi.org/10.5194/acp-23-13191-2023, 2023.

Kremser, S., Thomason, L. W., von Hobe, M., Hermann, M., Deshler, T., Timmreck, C., Toohey, M., Stenke, A., Schwarz, J. P., Weigel, R., Fueglistaler, S., Prata, F. J., Vernier, J.-P., Schlager, H., Barnes, J. E., Antuña-Marrero, J.-C., Fairlie, D., Palm, M., Mahieu, E., Notholt, J., Rex, M., Bingen, C., Vanhellemont, F., Bourassa, A., Plane, J. M. C., Klocke, D., Carn, S. A., Clarisse, L., Trickl, T., Neely, R., James, A. D., Rieger, L., Wilson, J. C., and Meland, B.: Stratospheric aerosol—Observations, processes, and impact on climate, Reviews of Geophysics, 54, 278–335, https://doi.org/10.1002/2015RG000511, 2016.

Lana, A., Bell, T. G., Simó, R., Vallina, S. M., Ballabrera-Poy, J., Kettle, A. J., Dachs, J., Bopp, L., Saltzman, E. S., Stefels, J., Johnson, J. E., and Liss, P. S.: An updated climatology of surface dimethlysulfide concentrations and emission fluxes in the global ocean, Global Biogeochemical Cycles, 25, https://doi.org/https://doi.org/10.1029/2010GB003850, 2011.

Li, C., Krotkov, N. A., Leonard, P., and Joiner, J.: OMI/Aura Sulphur Dioxide (SO2) Total Column 1-orbit L2 Swath 13x24 km V003, Goddard Earth Sciences Data and Information Services Center (GES DISC) [data set], https://doi.org/10.5067/Aura/OMI/DATA2022, 2020.

Malavelle, F. F., Haywood, J. M., Jones, A., Gettelman, A., Clarisse, L., Bauduin, S., Allan, R. P., Karset, I. H. H., Kristjánsson, J. E., Oreopoulos, L., Cho, N., Lee, D., Bellouin, N., Boucher, O., Grosvenor, D. P., Carslaw, K. S., Dhomse, S., Mann, G. W., Schmidt, A., Coe, H., Hartley, M. E., Dalvi, M., Hill, A. A., Johnson, B. T., Johnson, C. E., Knight, J. R., O'Connor, F. M., Partridge, D. G., Stier, P., Myhre, G., Platnick, S., Stephens, G. L., Takahashi, H., and Thordarson, T.: Strong constraints on aerosol–cloud interactions from volcanic eruptions, Nature, 546, 485–491, https://doi.org/10.1038/nature22974, 2017.

Mills, M. J., Schmidt, A., Easter, R., Solomon, S., Kinnison, D. E., Ghan, S. J., Neely III, R. R., Marsh, D. R., Conley, A., Bardeen, C. G., and Gettelman, A.: Global volcanic aerosol properties derived from emissions, 1990–2014, using CESM1(WACCM), Journal of Geophysical Research: Atmospheres, 121, 2332–2348, https://doi.org/10.1002/2015JD024290, 2016.

Montzka, S. A., Calvert, P., Hall, B. D., Elkins, J. W., Conway, T. J., Tans, P. P., and Sweeney, C.: On the global distribution, seasonality, and budget of atmospheric carbonyl sulfide (COS) and some similarities to CO2, Journal of Geophysical Research: Atmospheres, 112, https://doi.org/10.1029/2006JD007665, 2007.

Neely III, R. and Schmidt, A.: VolcanEESM: Global volcanic sulphur dioxide (SO2) emissions database from 1850 to present - Version 1.0 [Data set], https://doi.org/10.5285/76ebdc0b-0eed-4f70-b89e-55e606bcd568, 2016.

Pöschl, U., von Kuhlmann, R., Poisson, N., and Crutzen, P. J.: Development and intercomparison of condensed isoprene oxidation mechanisms for global atmospheric modeling, Journal of Atmospheric Chemistry, 37, 29–52, https://doi.org/10.1023/A:1006391009798, 2000.

Pozzer, A., Jöckel, P., Sander, R., Williams, J., Ganzeveld, L., and Lelieveld, J.: Technical Note: The MESSy-submodel AIRSEA calculating the air-sea exchange of chemical species, Atmospheric Chemistry and Physics, 6, 5435–5444, https://doi.org/10.5194/acp-6-5435-2006, 2006.

Pringle, K. J., Tost, H., Message, S., Steil, B., Giannadaki, D., Nenes, A., Fountoukis, C., Stier, P., Vignati, E., and Lelieveld, J.: Description and evaluation of GMXe: a new aerosol submodel for global simulations (v1), Geoscientific Model Development, 3, 391–412, https://doi.org/10.5194/gmd-3-391-2010, 2010.

Quaglia, I., Timmreck, C., Niemeier, U., Visioni, D., Pitari, G., Brodowsky, C., Brühl, C., Dhomse, S. S., Franke, H., Laakso, A., Mann, G. W., Rozanov, E., and Sukhodolov, T.: Interactive stratospheric aerosol models' response to different amounts and altitudes of SO_2 injection during the 1991 Pinatubo eruption, Atmospheric Chemistry and Physics, 23, 921–948, https://doi.org/10.5194/acp-23-921-2023, 2023.

Raspollini, P., Belotti, C., Burgess, A., Carli, B., Carlotti, M., Ceccherini, S., Dinelli, B. M., Dudhia, A., Flaud, J.-M., Funke, B., Höpfner, M., López-Puertas, M., Payne, V., Piccolo, C., Remedios, J. J., Ridolfi, M., and Spang, R.: MIPAS level 2 operational analysis, Atmospheric Chemistry and Physics, 6, 5605–5630, https://doi.org/10.5194/acp-6-5605-2006, 2006.

Reifenberg, S. F., Martin, A., Kohl, M., Bacer, S., Hamryszczak, Z., Tadic, I., Röder, L., Crowley, D. J., Fischer, H., Kaiser, K., Schneider, J., Dörich, R., Crowley, J. N., Tomsche, L., Marsing, A., Voigt, C., Zahn, A., Pöhlker, C., Holanda, B. A., Krüger, O., Pöschl, U., Pöhlker, M., Jöckel, P., Dorf, M., Schumann, U., Williams, J., Bohn, B., Curtius, J., Harder, H., Schlager, H., Lelieveld, J., and Pozzer, A.: Numerical

simulation of the impact of COVID-19 lockdown on tropospheric composition and aerosol radiative forcing in Europe, Atmospheric Chemistry and Physics, 22, 10 901–10 917, https://doi.org/10.5194/acp-22-10901-2022, 2022.

Rieger, L. A., Zawada, D. J., Bourassa, A. E., and Degenstein, D. A.: A Multiwavelength Retrieval Approach for Improved OSIRIS Aerosol Extinction Retrievals, Journal of Geophysical Research: Atmospheres, 124, 7286–7307, https://doi.org/10.1029/2018JD029897, 2019.

Rodgers, C. D.: Characterization and error analysis of profiles retrieved from remote sounding measurements, Journal of Geophysical Research: Atmospheres, 95, 5587–5595, https://doi.org/10.1029/JD095iD05p05587, 1990.

Rodgers, C. D. and Connor, B. J.: Intercomparison of remote sounding instruments, Journal of Geophysical Research: Atmospheres, 108, https://doi.org/10.1029/2002JD002299, 2003.

Roeckner, E., Bäuml, G., Bonaventura, L., Brokopf, R., Esch, M., Giorgetta, M., Hagemann, S., Kirchner, I., Kornblueh, L., Manzini, E., Schlese, U., and Schulzweida, U.: The atmospheric general circulation model ECHAM 5. PART I: Model description, Tech. rep., Max-Planck-Institut für Meteorologie, https://doi.org/10.17617/2.995269, 2003.

Ruder, S.: An overview of gradient descent optimization algorithms, arXiv preprint arXiv:1609.04747, 2016.

Sander, R., Baumgaertner, A., Cabrera-Perez, D., Frank, F., Gromov, S., Grooß, J.-U., Harder, H., Huijnen, V., Jöckel, P., Karydis, V. A., Niemeyer, K. E., Pozzer, A., Riede, H., Schultz, M. G., Taraborrelli, D., and Tauer, S.: The community atmospheric chemistry box model CAABA/MECCA-4.0, Geoscientific Model Development, 12, 1365–1385, https://doi.org/10.5194/gmd-12-1365-2019, 2019.

Schallock, J., Brühl, C., Bingen, C., Höpfner, M., Rieger, L., and Lelieveld, J.: Reconstructing volcanic radiative forcing since 1990, using a comprehensive emission inventory and spatially resolved sulfur injections from satellite data in a chemistry-climate model, Atmospheric Chemistry and Physics, 23, 1169–1207, https://doi.org/10.5194/acp-23-1169-2023, 2023.

Schmidt, A., Mills, M. J., Ghan, S., Gregory, J. M., Allan, R. P., Andrews, T., Bardeen, C. G., Conley, A., Forster, P. M., Gettelman, A., Portmann, R. W., Solomon, S., and Toon, O. B.: Volcanic Radiative Forcing From 1979 to 2015, Journal of Geophysical Research: Atmospheres, 123, 12 491–12 508, https://doi.org/10.1029/2018JD028776, 2018.

Schoeberl, M. R., Wang, Y., Ueyama, R., Taha, G., Jensen, E., and Yu, W.: Analysis and Impact of the Hunga Tonga-Hunga Ha'apai Stratospheric Water Vapor Plume, Geophysical Research Letters, 49, e2022GL100 248, https://doi.org/10.1029/2022GL100248, 2022.

Sellitto, P., Podglajen, A., Belhadji, R., Boichu, M., Carboni, E., Cuesta, J., Duchamp, C., Kloss, C., Siddans, R., Begue, N., Blare, L., Jegou, F., Khaykin, S., Renard, J.-B., and Legras, B.: The unexpected radiative impact of the Hunga Tonga eruption of 15th January 2022, Communications Earth & Environment, 3, 288, https://doi.org/10.1038/s43247-022-00618-z, 2022.

Stewart, C., Damby, D. E., Horwell, C. J., Elias, T., Ilyinskaya, E., Tomašek, I., Longo, B. M., Schmidt, A., Carlsen, H. K., Mason, E., Baxter, P. J., Cronin, S., and Witham, C.: Volcanic air pollution and human health: recent advances and future directions, Bulletin of Volcanology, 84, 11, https://doi.org/10.1007/s00445-021-01513-9, 2022.

Sun, K.: Derivation of Emissions From Satellite-Observed Column Amounts and Its Application to TROPOMI NO2 and CO Observations, Geophysical Research Letters, 49, e2022GL101 102, https://doi.org/https://doi.org/10.1029/2022GL101102, 2022.

Textor, C., Graf, H.-F., Timmreck, C., and Robock, A.: Emissions from volcanoes, in: Emissions of Atmospheric Trace Compounds, edited by Granier, C., Artaxo, P., and Reeves, C. E., pp. 269–303, Springer Netherlands, Dordrecht, https://doi.org/10.1007/978-1-4020-2167-1_7, 2004.

Theys, N., De Smedt, I., Yu, H., Danckaert, T., van Gent, J., Hörmann, C., Wagner, T., Hedelt, P., Bauer, H., Romahn, F., Pedergnana, M., Loyola, D., and Van Roozendael, M.: Sulfur dioxide retrievals from TROPOMI onboard Sentinel-5 Precursor: algorithm theoretical basis, Atmospheric Measurement Techniques, 10, 119–153, https://doi.org/10.5194/amt-10-119-2017, 2017.

Tie, X. and Brasseur, G.: The response of stratospheric ozone to volcanic eruptions: Sensitivity to atmospheric chlorine loading, Geophysical Research Letters, 22, 3035–3038, https://doi.org/10.1029/95GL03057, 1995.

Tilmes, S., Mills, M. J., Zhu, Y., Bardeen, C. G., Vitt, F., Yu, P., Fillmore, D., Liu, X., Toon, B., and Deshler, T.: Description and performance of a sectional aerosol microphysical model in the Community Earth System Model (CESM2), Geoscientific Model Development, 16, 6087–6125, https://doi.org/10.5194/gmd-16-6087-2023, 2023.

Timmreck, C., Mann, G. W., Aquila, V., Hommel, R., Lee, L. A., Schmidt, A., Brühl, C., Carn, S., Chin, M., Dhomse, S. S., Diehl, T., English, J. M., Mills, M. J., Neely, R., Sheng, J., Toohey, M., and Weisenstein, D.: The Interactive Stratospheric Aerosol Model Intercomparison Project (ISA-MIP): motivation and experimental design, Geoscientific Model Development, 11, 2581–2608, https://doi.org/10.5194/gmd-11-2581-2018, 2018.

Tost, H., Jöckel, P., Kerkweg, A., Sander, R., and Lelieveld, J.: Technical note: A new comprehensive SCAVenging submodel for global atmospheric chemistry modelling, Atmospheric Chemistry and Physics, 6, 565–574, https://doi.org/10.5194/acp-6-565-2006, 2006.

Vattioni, S., Stenke, A., Luo, B., Chiodo, G., Sukhodolov, T., Wunderlin, E., and Peter, T.: Importance of microphysical settings for climate forcing by stratospheric SO_2 injections as modeled by SOCOL-AERv2, Geoscientific Model Development, 17, 4181–4197, https://doi.org/10.5194/gmd-17-4181-2024, 2024.

Vehkamäki, H., Kulmala, M., Napari, I., Lehtinen, K. E. J., Timmreck, C., Noppel, M., and Laaksonen, A.: An improved parameterization for sulfuric acid–water nucleation rates for tropospheric and stratospheric conditions, Journal of Geophysical Research: Atmospheres, 107, AAC 3–1–AAC 3–10, https://doi.org/https://doi.org/10.1029/2002JD002184, 2002.

Vernier, J.-P., Thomason, L. W., Fairlie, T. D., Minnis, P., Palikonda, R., and Bedka, K. M.: Comment on "Large Volcanic Aerosol Load in the Stratosphere Linked to Asian Monsoon Transport", Science, 339, 647–647, https://doi.org/10.1126/science.1227817, 2013.

Vernier, J.-P., Fairlie, T. D., Deshler, T., Natarajan, M., Knepp, T., Foster, K., Wienhold, F. G., Bedka, K. M., Thomason, L., and Trepte, C.: In situ and space-based observations of the Kelud volcanic plume: The persistence of ash in the lower stratosphere, Journal of Geophysical Research: Atmospheres, 121, 11,104–11,118, https://doi.org/10.1002/2016JD025344, 2016.

Vömel, H., Evan, S., and Tully, M.: Water vapor injection into the stratosphere by Hunga Tonga-Hunga Ha'apai, Science, 377, 1444–1447, https://doi.org/10.1126/science.abq2299, 2022.

Xu, J., Li, D., Bai, Z., Tao, M., and Bian, J.: Large Amounts of Water Vapor Were Injected into the Stratosphere by the Hunga Tonga-Hunga Ha'apai Volcano Eruption, Atmosphere, 13, https://doi.org/10.3390/atmos13060912, 2022.

Zhu, Y., Toon, O. B., Jensen, E. J., Bardeen, C. G., Mills, M. J., Tolbert, M. A., Yu, P., and Woods, S.: Persisting volcanic ash particles impact stratospheric SO 2 lifetime and aerosol optical properties, Nature communications, 11, 1–11, https://doi.org/10.1038/s41467-020-18352-5, 2020.